Present-day strain distribution across a segment of the central bend of the North Anatolian Fault Zone from a Persistent-Scatterers InSAR analysis of the ERS and Envisat archives

M. Peyret, Frédéric Masson, Hakan Yavasoglu, Semih Ergintav, Robert Reilinger

Geophysical Journal International

Geophys. J. Int. (2013) **192,** 929–945 doi: 10.1093/gji/ggs085

Present-day strain distribution across a segment of the central bend of the North Anatolian Fault Zone from a Persistent-Scatterers InSAR analysis of the ERS and Envisat archives

M. Peyret,[1] F. Masson,[2] H. Yavasoglu,[3] S. Ergintav[4] and R. Reilinger[5]

[1] *Université Montpellier* 2, *Géosciences Montpellier, CNRS* UMR-5243, 34095 *Montpellier, France. E-mail: peyret@gm.univ-montp2.fr*
[2] IPGS-UMR7516, *EOST, Université de Strasbourg, INSU/CNRS, France*
[3] *ITU, Faculty of Civil Engineering, Department of Geomatics, Maslak-Istanbul, Turkey*
[4] *TUBITAK, Marmara Research Center, Earth and Marine Sciences Institute, Gebze* 41470, *Turkey*
[5] *Department of Earth, Atmospheric, and Planetary Sciences, Massachusetts Institute of Technology,* 77 *Massachusetts Ave, Cambridge, MA* 02139, *USA*

Accepted 2012 November 23. Received 2012 November 21; in original form 2012 March 20

SUMMARY

The North Anatolian Fault Zone (NAFZ) is the major transform system that accommodates the westward movement of the relatively rigid Anatolian block with respect to Eurasia. Mitigating the hazard associated with devastating earthquakes requires understanding how the NAFZ accumulates and releases the potential energy of elastic deformation both in space and in time. In this study, we focus on the central bend of the NAFZ where the strike of the North Anatolian Fault (NAF) changes from N75° to N105° within less than 100 km, and where a secondary fault system veers southwards within the interior of Anatolia. We present interseismic velocity fields obtained from a Persistent-Scatterers (PS) Interferometric radar analysis of ERS and Envisat radar archives. Despite the high vegetation cover, the spatial density of measurements is high (∼10 PS/km^2 in average). Interseismic velocities presented below indicate a velocity change of ∼6–8 mm/yr along the satellite line-of-sight (LOS) mainly centred on the NAF surface trace, and are in good agreement with the GPS velocity field published previously. The observed deformation is accommodated within a zone of ∼20 to 30 km width, in this area where no surface creep has been reported, contrary to the Ismetpasa segment located ∼30 km to the west of this study zone. Although less conspicuous, ∼2–3 mm/yr (∼1 mm/yr along the LOS) of the total deformation seems to be localized along the Lacin Fault. The overall agreement with horizontal GPS measurements suggests that the vertical component of the ground deformation is minor. This is confirmed, over the western part of our study zone, by the 3-D estimation of the ground deformation from the combination of the GPS- and the PS-mean velocity fields. However, a specific pattern of the PS velocity fields suggests that an area, enclosed between two faults with roughly south–north orientation, experiences uplift. The PS analyses of radar time-series both prior and posterior to the Izmit and Dûzce earthquakes indicate that these events did not induce detectable velocity changes in this central bend. The only temporal changes we identify are due to a moderate local earthquake (M_w 5.7, 1996 August 14) whose precise location and coseismic deformation are determined here. Finally, we propose a model of slip-rate distribution at depth along the NAF from the joint inversion of the GPS and PS mean velocity fields. This model suggests a long-term slip-rate of ∼20 mm/yr for a rather uniform locking depth in the range of 15–20 km. However, the locking depth increases to ∼25–30 km in the section comprised between longitudes E34°20' and E34°50'. This lateral evolution is in general agreement with the earthquake distribution at depth from three different catalogues.

Key words: Seismic cycle; Radar interferometry; Plate motions; Transform faults.

1 INTRODUCTION

The North Anatolian Fault Zone (NAFZ) extends approximately 1200 km from eastern Turkey to the northern Aegean Sea (Fig. 1). It is the major continental plate boundary transform system that separates the Anatolian Plate from the Eurasian Plate (e.g. Ambraseys 1970). It accommodates the westward movement of the roughly 'rigid' Anatolian block relatively to Eurasia (e.g. McKenzie

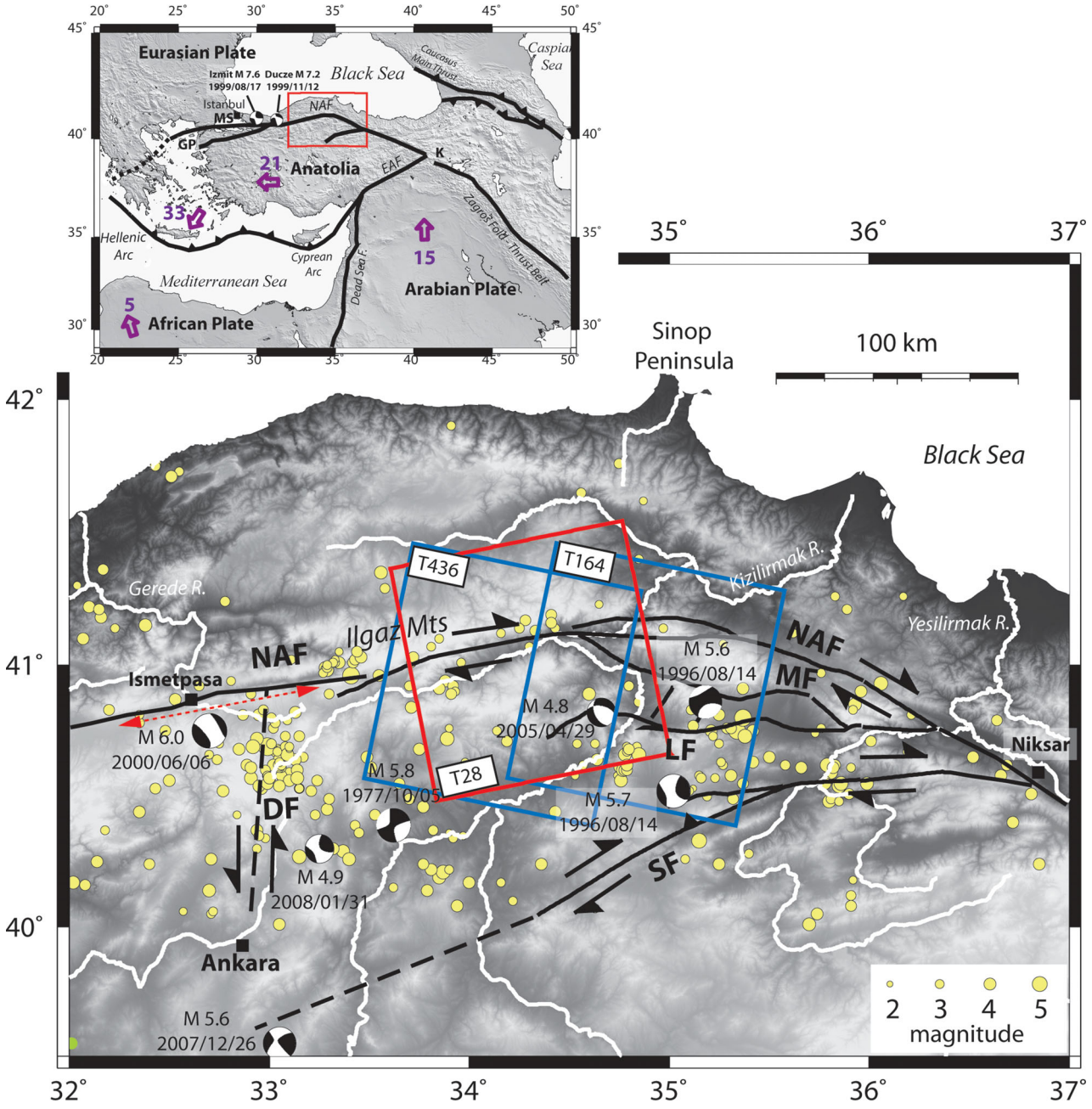

Figure 1. (Top) Simplified seismo-tectonic map of eastern Mediterranean and Middle East. Abbreviations are North Anatolian Fault (NAF), East Anatolian Fault (EAF), Karliova triple junction (K), Marmara Sea segment (MS) and Gelibolu Peninsula (GP). The red box shows the area covered by the figure below. Purple arrows and corresponding numbers show plate velocities (mm/yr) relative to fixed Eurasia, estimated from GPS velocities (Reilinger *et al.* 2006). (Bottom) Simplified seismo-tectonic map of the study zone. Focal mechanisms of earthquakes with magnitude higher than 4.5 since 1976, are from the Global CMT Project catalogue (www.globalcmt.org). The yellow circles show the location and magnitude (see size scale) of M>2 earthquakes since 1973 from the USGS catalogue. Abbreviations are Sungurlu Fault (SG), Lacin Fault (LF), Merzifon Fault (MF), Dodurga Fault (DF) and North Anatolian Fault (NAF). The red dotted arrow indicates the spatial extent of the Ismetpasa creep segment of the NAF (Cakir *et al.* 2005). The main rivers deflected by the NASZ are plotted in white. The footprints of the radar images are displayed with blue (descending pass) and red (ascending pass) squares whose side length is ∼100 km. Their track numbers are indicated within the white rectangles.

1972; Sengör *et al.* 2004). Its mechanism is predominantly right-lateral strike-slip from the Karliova triple junction to the Gelibolu peninsula.

Even though the North Anatolian Fault (NAF) exhibits a rather simple, single and uniform structure all along its trace, the present-day strain distribution across the NAF is likely not strictly uniform from East to West. Indeed, geometric or geologic conditions vary from one segment to another. Moreover, the temporal position within the seismic-cycle changes significantly. During the twentieth century, a sequence of eight extremely destructive earthquakes with magnitudes higher than 7.0 occurred on the NAFZ, taking the lives of over 50 000 residents and causing billions of dollars in property damage (e.g. Barka 1996; Stein *et al.* 1997). The central part of the NAFZ ruptured during the forties, whereas the recent Izmit (M 7.6, 1999/17/08) and Düzce (M 7.2, 1999/12/11) earthquakes hit the segment located to the east of the Marmara Sea. None of the large

earthquakes of the twentieth century occurred on the Marmara Sea segment of the NAFZ (Fig. 1).

Understanding the way the NAF accumulates and releases the potential energy of elastic deformation both in space and in time is important as it bears directly on the problem of estimating and mitigating the hazard associated with devastating earthquakes. Satellite geodetic techniques allow determination of crustal deformation with subcentimetre precision. This permits us to estimate the present-day tectonic loading on a fault, and the associated fault mechanical behaviour (i.e. slip rates and orientations, locking depths, fault dip, and variations in these parameters along strike).

In this study, we focus on the central segment of the NAFZ roughly located between longitudes E33° and E36° (Fig. 1). Within less than one hundred kilometres, the strike of the NAFZ changes from N75° to N105°. Moreover, in this area, in contrast to over most of the NAFZ length, an important secondary fault system exists to the south. Even though, historical and instrumental records indicate that it is active (e.g. Ambraseys 2009), its present role in strain accommodation is thought to be minor as attested by recent GPS measurements (Yavasoglu *et al.* 2006). However, this still needs to be assessed with complementary observations. The major restraining bend in this central segment of the NAFZ is likely to induce along-strike variations in strain distribution and fault behaviour.

Our study zone is located ∼400 km east of the Düzce rupture. Ergintav *et al.* (2009) have established that their easternmost GPS site in Ankara, which is the closest to our study area (∼50 km to the west), exhibits a slowly decaying postseismic velocity following the Izmit-Düzce earthquake sequence. This transient is modelled by a logarithmic decay with a time constant of about 10 yr. Therefore, the postseismic velocity of the site of Ankara evolves from ∼5 mm/yr just after the earthquake sequence to ∼2 mm/yr 10 yr later. Assuming a symmetric pattern across the NAF, the mean relative postseismic motion across the NAF over the 10 yr following the earthquakes can be estimated to ∼7 mm/yr at the longitude of Ankara (i.e. ∼2 mm/yr along the radar satellite line-of-sight). This value can be considered as the upper bound of the relative post-seismic motion that one can expect in our study zone. Therefore, even though one may predict that the post-seismic strain gradient in the central bend, as well as its temporal evolution, is likely negligible with respect to the interseismic strain field, this needs to be ascertained with direct measurements.

Finally, west of longitude E33°, the NAF exhibits some shallow creep (Cakir *et al.* 2005; Kutoglu *et al.* 2008; Fialko *et al.* 2011). However, surface creep has not been reported within our study zone.

To address the question of the character of tectonic loading of this central segment and how loading is accommodated by the NAFZ, we first summarize the basic seismo-tectonic setting of the study area. Then we present the interseismic mean-velocity fields deduced from a 'persistent-scatterers' radar interferometric analysis (PSI) of ERS and Envisat radar archives. We present the ground deformation associated with the Salhan Çayı earthquake (Mw 5.7, 1996 August 14), and establish the similarity of deformation prior and after the Izmit and Düzce earthquakes. Then, we use a two-step inversion procedure for estimating both the distribution of slip-rate deficit and the locking depths of the NAF from the PS velocity fields. Finally, this model is compared with seismicity.

2 TECTONIC AND SEISMIC SETTINGS

The convergence between the African and Eurasian plates in the eastern Mediterranean results in the westward extrusion of the Anatolian block (Fig. 1). The increasing rates of motion of the Anatolian plate towards the west suggest that forces resulting from the subduction of the African plate along the Hellenic and Cyprus Arcs are the main forces that drive its motion (e.g. McClusky *et al.* 2000; Wortel & Spakman 2000). The Anatolian plate is not deforming very much (e.g. Aktug *et al.* 2009), and thus behaves as a quasi-rigid block. The NAFZ bounds the Anatolian plate to the north. Its width, which is about 100 km, regularly increases from east to west, even though some pinched or swelled zones exist (Sengör *et al.* 2004). Its arched form, as well as its position which closely matches a small circle, illustrates the approximately rigid rotation of the Anatolian block with respect to Eurasia, around an Euler pole located in northern Egypt (e.g. McClusky *et al.* 2000; Reilinger *et al.* 2006).

Geologic evidence suggests that the NAF formed at about 13 to 11 Ma in the east and propagated westwards at ∼11 cm/yr (Sengör *et al.* 2004). The fault is located along an interface that separates subduction-accretion material to the south, from the older and stiffer continental basement to the north (Sengör *et al.* 2004). To the east, the NAFZ connects to the East Anatolian Fault Zone (EAFZ) at the Karliova triple junction. West of longitude E32°, the NAF divides into two main strands. The northern one lies beneath the Marmara Sea and reaches the Gulf of Saros, while the southern strand passes south of the Marmara Sea. Very few fault systems seem to transfer deformation within the Anatolian block. An important exception occurs along the central part of the NAF, notably in our study area, southeast of the central bend. It consists of splay faults extending southwards within the inner Anatolia block.

The main, active trace of the NAFZ has a sharp morphological expression. Large-scale structural offsets have been estimated in the Pontide suture located close to the city of Erzincan (longitude E39°20') (Bergougnan 1975; Sengör *et al.* 1985), around the Sea of Marmara (Armijo *et al.* 1999) and in the western part of the central bend (Hubert-Ferrari *et al.* 2002). They all amount to about 80 km. This cumulative displacement along the NAF is confirmed by the analysis of major river deflections, including the Yesilirmak, Kizilirmak and Gerede rivers (Fig. 1) (Hubert-Ferrari *et al.* 2002; Sengör *et al.* 2004). Furthermore, measuring and dating stream channel offsets lead to geological slip rate estimates of ∼18 mm/yr (Hubert-Ferrari *et al.* 2002) to 20.5 mm/yr (Kozaci *et al.* 2007) that can be compared to present-day slip motion estimated from rigid block modelling of GPS measurements of about 17 to 25 mm/yr (e.g. Reilinger *et al.* 1997, 2006; Straub *et al.* 1997; McClusky *et al.* 2000; Provost *et al.* 2003).

In this study, we focus on the central segment of the NAFZ bounded by longitudes E33° and E36°. In this Tokat lobe of the Tethyside accretionary complexes, the suture between the subduction-accretion material and the continental basement rocks is located further north of the fault trace (Sengör *et al.* 2004). While this change in material strength may induce some asymmetric pattern in the strain distribution induced by tectonic loading elsewhere along the NAFZ (e.g. Sengör *et al.* 2004), it will likely have a lesser effect in this study zone.

The NAF orientation rotates by about 30° from N75° at longitude E33°, to N105° at longitude E36°. This area is characterized by the existence of a secondary large horsetail fault system (Fig. 1) that develops south of the NAF from the city of Niksar (Fig. 1). It roughly strikes parallel to the main NAF strand and consists of southward-splitting concave branches. Among the major branches are the Sungurlu (also referred to as Ezinepazari), Merzifon and Lacin faults (e.g. Barka *et al.* 2000; Hubert-Ferrari *et al.* 2002; Yavasoglu *et al.* 2006, 2011). Palaeomagnetic data indicate that the Sungurlu fault is a boundary between anticlockwise (to the south)

and clockwise (to the north) block rotations (Isseven & Tüysüz 2006).

This segment of the NAF was ruptured by the very large 1668 earthquake (e.g. Ambraseys 2009; magnitude estimated to 8.0 in the USGS catalogue of historical seismicity) and a 1939–1943–1944 westward sequence of $M > 7$ earthquakes, the largest being the $M = 7.3$, 1943 Tosya earthquake (e.g. Ambraseys 1970, 2009; Barka 1996; Yoshioka *et al.* 2000; Hartleb *et al.* 2003). A temporal seismic gap seems to separate the 1668 and 1943 events. Despite the several decades since the most recent large earthquakes, non-negligible post-seismic deformation may still affect present-day ground deformation (Hearn *et al.* 2002).

Some studies suggest that some post-seismic deformation induced by the recent Izmit and Düzce earthquakes may also affect this central part of the NAF (Ergintav *et al.* 2009; Hearn *et al.* 2009). Nevertheless, as discussed above, we suspect that in this region and during the period of SAR coverage (2004–2010) the amplitude of the post-seismic strain gradients should remain within the radar measurements uncertainty, and, in any case, significantly lower than that induced by interseismic loading.

Most of the present-day seismic activity is essentially limited to south of the NAFZ (Fig. 1). Historical and instrumental seismic records indicate that the southern, secondary branches are active. More precisely, seismicity appears to be mainly distributed throughout the area bounded by the NAFZ to the north, and the Sungurlu fault to the south (Fig. 1). Some focal mechanisms exhibit significant normal or thrust components in addition to the predominant dextral strike-slip.

The mode of deformation of the NAFZ is essentially pure right-lateral strike-slip all along its trace. However, in this central part, the fault bend does not follow a small circle but is rather parallel to the Black Sea coastline. Consequently, this central restraining bend causes significant changes in the fault-normal component of deformation. Geological and geomorphological observations in the Ilgaz Moutains area (Fig. 1) indicate active compressive deformation (e.g. Barka 1992). In this area, the mode of deformation is transpressive (e.g. Sengör *et al.* 2004), whereas, further west, the mode of deformation becomes trans-tension. The way these deformations are partitioned is still being debated.

To complement the global GPS networks on the scale of the Eastern Mediterranean whose primary aim is to focus on the global extrusion of the Anatolian block and the corresponding large-scale behaviour of the NAFZ and EAFZ (e.g. Reilinger *et al.* 1997, 2006; Kahle *et al.* 2000; McClusky *et al.* 2000, 2003; Hearn *et al.* 2002), denser regional networks have been installed over different segments of the NAFZ (e.g. Delouis *et al.* 2002; Ergintav *et al.* 2002; Tatar *et al.* 2012). In this study, we will use the horizontal GPS velocity field published by Yavasoglu *et al.* (2011) as a reference velocity field of the study region. It covers a large part of our study zone, and the velocities have been estimated from 4 GPS surveys performed between 2001 and 2005.

3 PERSISTENT-SCATTERERS InSAR ANALYSIS

3.1 Methodology and data sets

The low spatial density of GPS networks (with typical baselines of several tens of kilometres) makes this technique inefficient for mapping spatially heterogeneous ground deformation patterns, especially at short spatial scale (e.g. local anthropogenic effects, or near-field deformation for a fault at any stage of the seismic-cycle). Moreover, GPS measurement of the vertical component of displacement is about a factor of 3–5 (higher for short observation sessions) less precise than the horizontal (for relatively long sessions, 2.5–7 mm for vertical compared to 1–2 mm for horizontal). Therefore, an accurate estimation of the vertical displacement rate will require several GPS campaigns separated by long time intervals. For these reasons, the radar interferometry (InSAR) technique (e.g. Massonnet & Feigl 1998; Bürgmann *et al.* 2000) is an ideal complementary approach to GPS for crustal deformation studies. Indeed, theoretically it provides spatially dense (decametre scale) measurements of ground deformation with subcentimetre precision. Nevertheless, InSAR is only sensitive to the component of deformation along the satellite line-of-sight (LOS), that is to say most sensitive to east-west and vertical motion for existing satellites in near-polar orbits. In our study area, this geometric configuration is favourable for measuring any vertical or fault-parallel displacement.

In practice, InSAR requires the conservation of geometrical and physical properties of homologous pixels between a pair of satellite acquisitions (Zebker & Villasenor 1992). For radar systems using electromagnetic waves in the C-band range, like the ones onboard the ERS and Envisat satellites, the main source of decorrelation is the vegetation coverage. This loss of coherence generally increases with time and seasonal difference. Thus, InSAR technique often fails to map long-term ground deformation. This is particularly true for the northern Turkey which exhibits dense vegetation.

The second significant limitation to ground-deformation analysis by InSAR is the interferometric phase delay due to relative changes in atmospheric conditions between the two acquisitions (e.g. Zebker *et al.* 1997). This effect adds spatially coherent noise on phase at spatial scales ranging from several hundred metres to tens of kilometres (e.g. Emardson *et al.* 2003). The typical amplitude of these artefacts is about one fringe (a few cm). Consequently, it is often difficult to discriminate small, distributed ground-deformation gradients (typically $\sim$20 mm / 30 km in line of sight, i.e. $\sim 10^{-2}$ fringe/km, for interseismic elastic deformation) from fringe patterns of different origins.

Due to these two major limitations, standard-InSAR analyses of the interseismic deformation along the NAF are sparse. Some have focused on the arid eastern end of the NAFZ (Wright *et al.* 2001; Walters *et al.* 2011), while another study was limited to the surface creeping zone of the Ismetpasa fault segment (Cakir *et al.* 2005). However, despite its lower precision than C-band data, the use of ALOS L-Band acquisitions now allows elimination of most of the decorrelation due to vegetation (Fialko *et al.* 2011). Yet, these archives only span $\sim$3 yr and thus provide shorter time-series than ERS or Envisat.

Hence, determining the interseismic deformation that affects our study zone from C-band radar archives of ERS and Envisat, requires implementing a more sophisticated approach to interferometric phase analysis. Even though a SBAS technique could also be effective (e.g. Bernardino *et al.* 2002), we implemented the 'Permanent-Scatterers' (PS-InSAR®) or 'Persistent-Scatterers' InSAR (PSI) approach.

The PS-InSAR or PSI principle was originally defined by Ferretti *et al.* (1999, 2001). It acknowledges the fact that, within spatially decorrelated areas, some pixels may exhibit some phase stability over a time-series of interferograms. For such pixels, called 'permanent' or 'persistent' scatterers (PS), one individual scatterer generally dominates the echo. Hence, PS pixels behave like point scatterers and decorrelation is greatly reduced.

Different criteria may be used for identifying PS pixels. The amplitude dispersion index and the signal-to-clutter ratio have been

widely used (e.g. Ferretti *et al.* 2001; Adam *et al.* 2004). They proved to be good proxies for phase standard deviation, but solely for high signal-to-noise ratio. Thus, many PS analyses are mainly restricted to man-made structures or urban areas. Furthermore, many PS-InSAR and PSI algorithms consider that the phase history of a PS must also match an assumed model of how displacement varies with time (e.g. Ferretti *et al.* 1999, 2001; Lyons & Sandwell 2003; Werner *et al.* 2003; Adam *et al.* 2004; Kampes 2005).

In this study, we use the 'StaMPS' (Stanford Method for Persistent Scatterers) PSI method (Hooper *et al.* 2004, 2007; Hooper 2006). Contrary to most PS selection strategies, StaMPS uses spatial correlation of phase measurements to identify PS pixels (e.g. Hooper *et al.* 2004; Van der Kooij *et al.* 2005). The probability for a pixel to be a PS is estimated through a phase analysis which is successively refined in a series of iterations. This strategy allows the detection of PS pixels even if their amplitude is low, which is often the case in natural terrains, and without any prior assumption about the temporal nature of the ground deformation. Instead of requiring a known temporal dependence of deformation, StaMPS simply utilizes the spatially correlated nature of the deformation.

However, a random phased pixel may produce a phase time-series that appears to be coherent. Such pixels are called false-PS. The analysis of the histograms of temporal coherence obtained from both the data and a large set of simulated random phase sequences, allows for the estimation of the probability density function of a pixel to be a real- or a false-PS (Hooper 2006). All the radar time-series presented throughout this paper have been processed with a threshold of random false-PS percent (PR) equal to 5 per cent. The choice of such a low threshold aims for a reliable selection of PS. Therefore, we expect PS mean velocity fields globally free of significant artefact, even though one cannot completely rule them out.

Once a PS data set has been determined, the PS-InSAR and PSI processing consists of analyzing the phase time-series for all the PS pixels. This involves removing the residual topographic component of the flattened interferograms, and then unwrapping the phase both spatially and temporally. This analysis enables the extraction of the deformation component of the radar signal, including a step in which most of the atmospheric signal is estimated and removed.

In this study, the differential interferograms have been constructed with 'Roi_pac' (Rosen *et al.* 2004) and 'Doris' softwares (Kampes *et al.* 2003). We used precise ERS orbits from Delft (Kampes *et al.* 2003). We flattened and georeferenced the interferograms using the SRTM digital elevation model (Farr *et al.* 2007) that we over-sampled to 1.5 s. Finally, looking at interseismic InSAR results requires the removal of any orbital error without affecting the long spatial wavelength of the ground deformation signal. A usual approach consists in adjusting the far-field deformation (in presumed undeformed zones) to the null-deformation (e.g. Fialko 2006), processing consecutive frames if necessary (e.g. Wright *et al.* 2001). In this study, we optimize (in a weighted least-square sense) the spatially linear transform that best fits the PS velocity field (in the vicinity of GPS sites) to the GPS velocity field projected along the satellite LOS. This allows converting the PS velocity field into the fixed Eurasia reference frame, while removing any possible effects of orbital errors. Despite the low density of the GPS network, especially north of the NAF, we control that this final adjustment leads to gradients of PS velocities that are null beyond a few tens of kilometres from the main faults. Finally, in the following paragraphs, we present values of correlation between PS and GPS measurements that are in fact the correlation between the deviations of these data sets from their own best fit plane. In this way, this correlation parameter is not biased by our adjustment of the PS velocity fields to the GPS measurements.

We present here the results of the PSI analysis of the ERS and Envisat radar archives acquired on three different frames (Fig. 1).

3.2 PS mean-velocity field for the eastern zone (from lon. 34°20' to 35°40')

This eastern part of the central bend (Fig. 1) has been imaged by the Envisat satellite in its descending pass along frame 2780 and track 164. The radar images data set consists of 43 images (Fig. A1). The master image (2007 November 10) has been chosen so that it roughly minimizes the sum, over the whole set of slave images, of the perpendicular baselines and the time intervals. No significant earthquake (M>5) has occurred during the time interval spanned by these archives (2003 September to 2010 August). So, we consider that the PS mean-velocity field can be compared with the GPS velocity field obtained by Yavasoglu *et al.* (2011).

Fig. 2 shows the PS mean-velocity field (along the LOS) deduced from the PSI analysis of this radar time-series. Despite the heavy constraint on false-PS selection (PR = 5 per cent), 39835 PS have been detected. This corresponds to a mean spatial density of about 6 PS/km^2. However, this density significantly decreases over most of the steeply sloping and highly vegetated areas (essentially constituted of forests), and over the Merzifon plain probably because of agricultural activity.

The mean PS-velocity change across the NAFZ is estimated to 8 ± 1 mm/yr in the LOS direction. If one considers that the ground displacement is essentially parallel to the fault strike (± 15° relative to the east-west direction), then 8 mm/yr in the mean LOS direction corresponds to 20–23 ± 2–3 mm/yr on the ground. This estimation fully agrees with velocity gradients estimated from GPS as

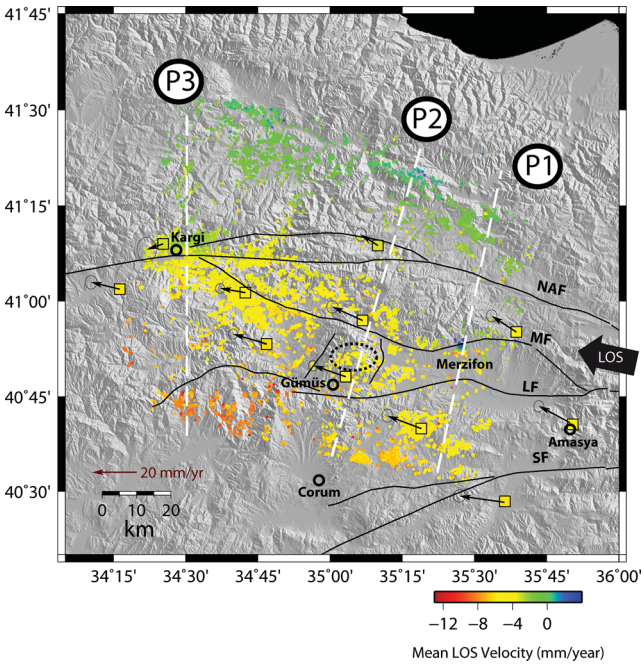

Figure 2. PS mean velocity map from Envisat archives in descending orbits on the eastern frame. GPS velocity field with 95 per cent confidence ellipses is from Yavasoglu *et al.* (2011). Coloured squares at GPS sites represent the GPS velocities projected onto the satellite LOS. Profiles used in Fig. 3 are plotted with dashed white lines. The black dotted line shows the location of the area that is likely slightly uplifting. Abbreviations as in Fig. 1.

evidenced in Fig. 2 by the projection of the GPS velocities along the satellite LOS. The correlation between these two velocity fields is quite good, leading to an RMS of 0.7 mm/yr (Fig. A7b). This RMS is lower than the uncertainties associated with both GPS ($\sigma-1$ uncertainty $\sim$1.0 mm/yr) and PS measurements whose mean velocity disparity is $\sim$0.7 mm/yr, roughly uniformly all over the imaged zone. However, the low spatial density of the GPS network makes this RMS (and the other RMS presented hereafter) just indicative of the global coherence of the PS and GPS data sets rather than an obvious evidence of the reliability of the whole PS velocity field. Nevertheless, this good fit suggests that the vertical component of the deformation (well captured by InSAR, but not determined in the solely horizontal GPS velocity field of Yavasoglu *et al.* (2011)) is negligible (typically, lower than 1 mm/yr). Moreover, all the PS phase time-series indicate a high steadiness of the deformation throughout the period spanned by the radar acquisitions. Thus, no detectable transient deformation (typically inducing a gradual-in-time evolution of the ground velocity of at least 2 mm/yr LOS over the time spanned by the archives) seems to affect this zone.

Throughout the rest of this paper, PS velocity disparities are taken as a first-order proxy for PS velocity uncertainties. All the PS velocity fields we present exhibit a mean velocity disparity of $\sim$1 mm/yr implying uncertainties on PS velocity measurements of the order of 1 mm/yr LOS.

Fig. 2 highlights the diffuse aspect of the ground deformation across the NAFZ. Even though one can note velocity gradients across the NAFZ and, to a lesser degree, the LF, they occur gradually. This complies with the absence of surface creep reported in this area. Only one single pattern of highly localized deformation occurs just over the city of Merzifon (N35°33', E40°48'). This displacement of the ground is away from the satellite in its southern part and towards the satellite in its northern part, most likely associated with subsidence and uplift respectively. Even though this deformation occurs right across the Merzifon fault, it has probably an anthropogenic origin. This may be related to water pumping like in the vicinity of numerous large cities in arid areas (e.g. Motagh *et al.* 2007a). Nevertheless, despite the low density of PS out of the Merzifon city, this ground deformation seems to affect only the alluvial fan over which the city of Merzifon is built (Fig. A6), and which is located downstream the Yakacik dam ($\sim$2 km north-west of the city). Hence, this deformation is likely associated with the dynamic response of this alluvial fan to the load and discharge of this dam.

In order to illustrate better the results of our InSAR analysis, we plot PS-velocities and GPS-velocities (projected along the satellite LOS) along three profiles roughly perpendicular to the NAFZ (Figs 2 and 3). PS- and GPS-velocities are plotted for PS located no more than 3 km distance from the profiles, and GPS sites located no more than 20 km distance from the profiles.

The first profile (P1) is located in the eastern part of the scene with a N20E° orientation. It passes through the deforming zone of the city of Merzifon discussed previously (section between 35 km and 45 km of profile P1 on Fig. 3). Despite the lack of PS, especially on the southern edge of the NAFZ, this profile confirms that 80 per cent of the far-field rate (5 $\pm$ 1 mm/yr along LOS) is accommodated by the NAFZ within a distance of $\sim$30 $\pm$ 10 km (approximately between 45 and 75 km). The gradient of deformation becomes quasi-null $\sim$10 km north of the NAFZ and south of the LF.

The second profile (P2), located about 35 km more to the west, has a N20E° orientation and passes close to 3 GPS sites. Once again, the main gradient of deformation occurs across the NAFZ. Its amplitude has slightly increased from 5 $\pm$ 1 mm/yr for P1 to 6 $\pm$ 1 mm/yr. 80 per cent of this deformation is still accommodated within $\sim$30 $\pm$ 10 km (approximately between 50 and 80 km along the profile P2). By going southwards, a pattern of velocity increase of 1 $\pm$ 1 mm/yr appears south of the Merzifon fault (30 km on profile), on the south-eastern flank of the topography that borders the Merzifon basin to the west (see dotted line on Fig. 2). It can hardly be interpreted as a horizontal velocity change since this would imply a left-lateral mechanism for the Merzifon fault that is inconsistent with the regional right-lateral strike-slip tectonic context. This pattern could also be interpreted as an atmospheric residue of the PSI analysis correlated with the local topography. Nevertheless, such a correlation is not observed over the neighbouring mountains (see for example the null deformation estimated along the hilly southern section of profile P2, between 0 km and 20 km). More generally, this kind of artefact is not observed in any other place and any other data set processed in this study. Hence, even though one cannot definitely rule out this latter interpretation, this velocity change probably expresses a local uplift. Finally, a slight (1 $\pm$ 1 mm/yr) change of the PS-velocity occurs around 20 km on profile. This additional deformation is localized close to the Lacin Fault.

About 50 km further west, the western profile (P3), with north-south orientation, reveals a clear velocity gradient centred on the surface trace of the NAF. 80 per cent of the complete deformation (6 $\pm$ 1 mm/yr) seems to be accommodated within 20 $\pm$ 10 km (approximately between 40 and 60 km). Despite the uncertainty associated with these PS mean velocities, a possible faint asymmetry of the velocity gradients across the NAFZ can be noted. If so, it could reveal that the northern side of the NAFZ would be more deforming than the southern side, and/or that the fault is dipping to the North. Finally, as noted above, a faint (1 $\pm$ 1 mm/yr) velocity change occurs across the Lacin fault zone.

Briefly summarizing the information provided by this PS-velocity map, we first observe that the ground deformation is quite steady with time, and the major velocity change (6 $\pm$ 1 mm/yr along the LOS) occurs across the NAFZ within a width of $\sim$20–30 $\pm$ 10 km. Finally, to the south, 1$\pm$ 1 mm/yr of LOS velocity offset appears to be localized close to the Lacin Fault, essentially west of longitude 35°00'.

3.3 Salhan Çayi earthquake (M_w 5.7, 1996 August 14) and the interseismic deformation prior 1999

In order to explore the relative change of velocity that could have been induced by the Izmit (M_w 7.6, 1999 August 17) and the Düzce (M_w 7.2, 1999 November 12) earthquakes on the same track as the previous Envisat data set, we processed the ERS radar images time-series that spans the period 1992 May to 1999 November (Fig. A2). However, this area was struck by a moderate earthquake (M_w 5.7) on 1996 August 14. This event, referred to as the Salan Çayi earthquake (Rojay & Koçyiğit 2011), is thought to have ruptured a segment of the Lacin Fault, along the south-western border of the Merzifon-Suluova pull-apart basin (Fig. 4a). No surface rupture or deformation induced by this earthquake has been reported, except a landslide and some damage in Amasya (N40°39', E35°50') (USGS catalogue). The differential radar interferograms spanning this event reveal some faint phase changes in the expected zone of rupture. Nevertheless, these patterns are almost completely obscured by the atmospheric delays and the spatial and temporal decorrelation.

The PSI processing of the whole time-series not only estimates the mean velocity for each PS, but also provides a time-series of the PS position as estimated after correction of atmospheric delays and topographic errors. Despite the low temporal density of these

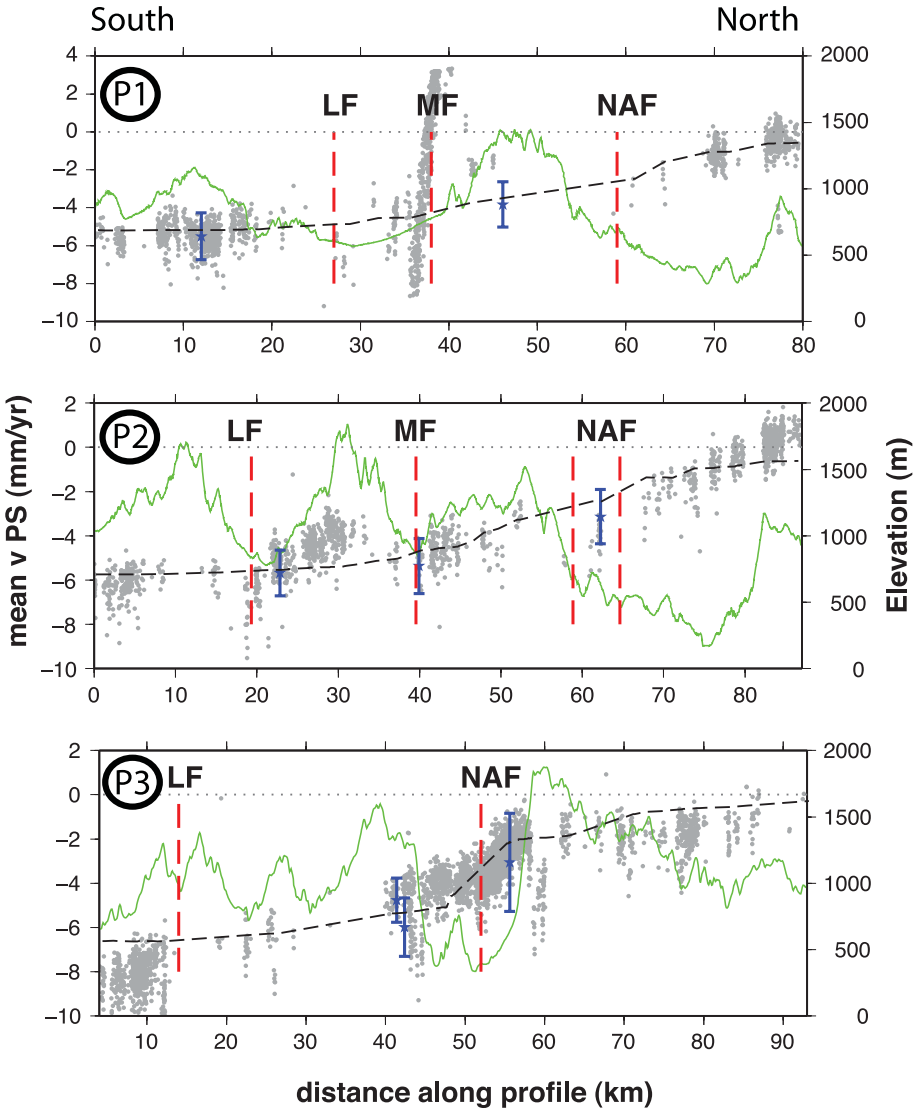

Figure 3. Comparison of GPS velocities along the satellite LOS (blue stars with error bars) and PS mean velocities (grey circles) for the three profiles whose locations are shown in Fig. 2. PS are selected within a ± 3 km distance from the profile. GPS are selected within a ± 20 km distance from the profile. The locations of the faults along the profiles are indicated with red vertical dashed lines. Topography along the profile is shown in green curve. The black dotted line indicates the LOS velocity profile predicted by our slip-rate model at depth described in paragraph 4. Abbreviations as in Fig. 1.

archives, a detailed analysis of the individual time-series reveals significant position offsets for the PS located close to (N40°40', E35°20'). Fig. 4b illustrates this with PS whose locations are indicated on Fig. 4c with black arrows. The northern PS exhibit a positive offset (towards the satellite located eastwards) of ∼2–3 cm with respect to the position expected from the position evolution prior the Salhan Çayi earthquake (in these plots, the PS mean velocities have not been adjusted to the GPS velocity reference frame). Conversely, southern PS display a negative offset (away from the satellite) of ∼5 cm. Such significant offsets do not exist for PS situated at distances greater than ∼20 km from this area.

One considers that, as stated by the previous Envisat data set analysis, only a negligible interseismic motion across the fault over 3–4 yr is expected and that no significant postseismic deformation occurred. Then, simply differencing the average pre- and post-earthquake positions, and plotting their relative values allows estimating the coseismic offset from the radar time-series. This processing leads to the coseismic displacement field presented on Fig. 4c. Alternative approaches for computing such a displacement field without orbital and interseismic residues have been developed (e.g. Manzo *et al.* 2011). We provide a very basic alternative approach in Appendix. Its implementation leads to a coseismic displacement field similar to the one presented on Fig. 4c and discussed below.

As estimated from individual time-series, the peak amplitude of ground displacement is ∼10 cm along LOS. This would correspond to ∼30 cm of east–west horizontal displacement for a quasi-pure strike-slip event. This is the order of magnitude of ground displacement expected for such a moderate earthquake (e.g. Lohman & Simons 2005). It should be noted, however, that, in the case of such a moderate event, it is difficult, if not impossible, to determine whether the rupture occurred along the primary or the auxiliary nodal plane (e.g. Taymaz *et al.* 2004; Biggs *et al.* 2006). Therefore, the rupture could be oriented S-N and the ∼10 cm of LOS displacement would now correspond to ∼100 cm on the ground which may

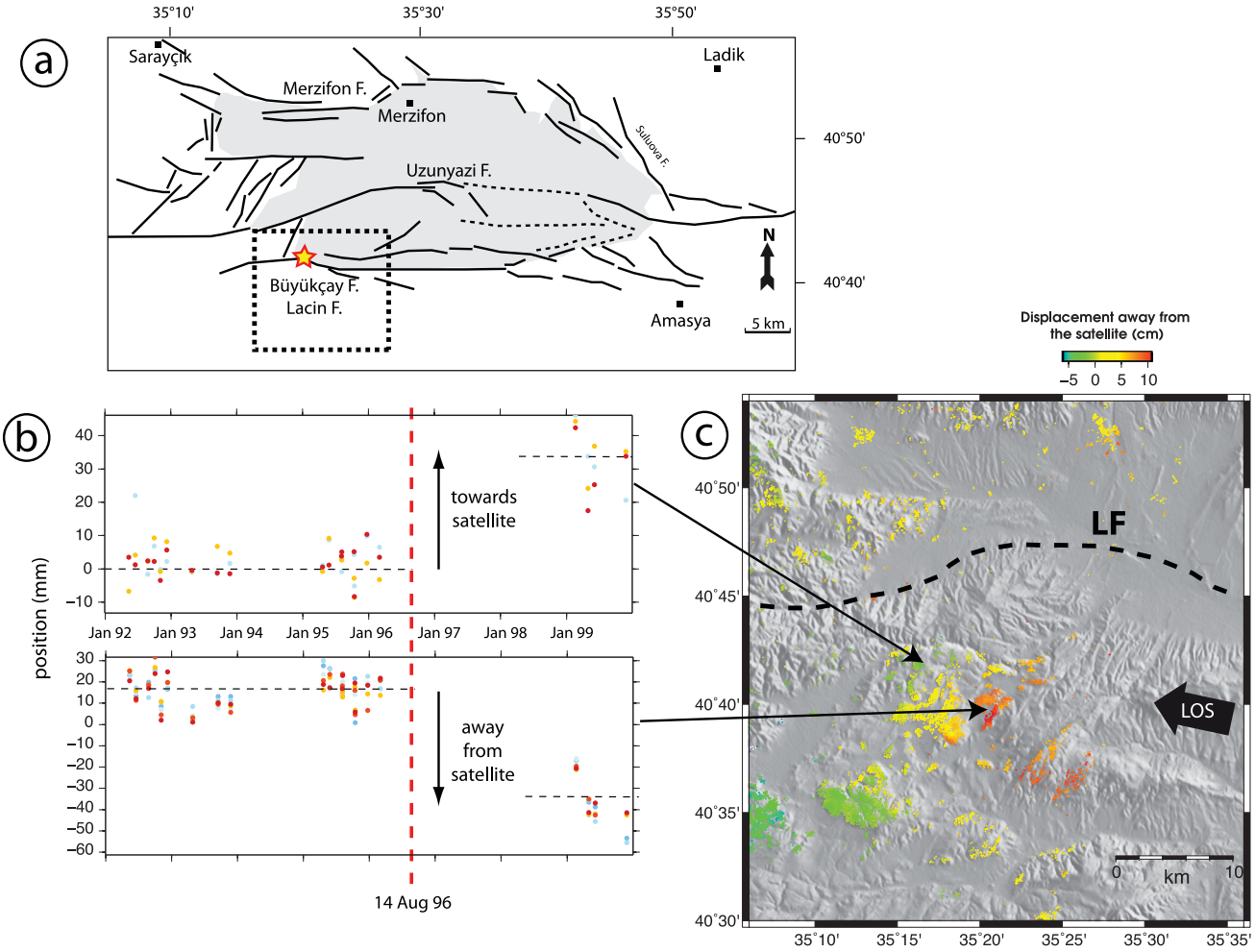

Figure 4. (a) Simplified neo-tectonic map of the Merzifon-Suluova basin from fig. 3 of Rojay & Koçyiğit (2011). Grey area corresponds to Plio-Quaternary fill. The location of the Salhan Çayi earthquake is shown with the yellow star. (b) Evolution of PS position along the ERS time-series for PS located on both sides of the fault segment that ruptured during the Salhan Çayi earthquake (see corresponding spatial location on map (c) indicated with the black arrows). Each PS is associated with one specific colour of symbol. (c) Salhan Çayi coseismic displacement map estimated from the difference of the average pre- and post-earthquake positions.

appear too much when considering that no significant surface rupture has been reported. Although, the uncertainty associated with these amplitudes is rather high (∼2 cm) due in particular to the low density of the time-series after the Salhan Çayi earthquake, the highest gradients of LOS displacement (∼10 cm within 4 km) clearly identify the location of the fault segment that ruptured. Surprisingly, it does not occur on the main Lacin Fault segment whose surface trace is plotted with a black dotted line on Fig. 4c, but rather on a subparallel branch that lies on the southern foot of the topography that borders the Merzifon plain to the south-west.

Thus, the Salhan Çayi event significantly alters the presumed steady time-evolution of PS positions due to interseismic loading. Therefore, we limited the ERS archives to acquisitions before this earthquake. The PSI processing of the pre-Salhan Çayi earthquake radar time-series leads to a PS-mean velocity field (Fig. A8) that is similar to the velocity field obtained from the Envisat archives, within the high uncertainties (± ∼2 mm/yr) due to the rather small temporal length and density of this time-series. In particular, one gets confirmation (1) of the deformation over the city of Merzifon, (2) of the global shape and amplitude of the main gradient of deformation centred on the NAF, and (3) of the existence of a slight gradient of deformation close to the LF. On the contrary, the high uncertainty associated with this PS velocity field does not allow for the confirmation or the refutation of the possible uplift north of the Gümüs Village and the possible asymmetry of the deformation across the NAFZ observed on profile P3. This global similarity suggests that the postseismic deformation induced by the Izmit and the Düzce earthquakes has not modified the regional mean velocity field to the extent that it could be detected by our analysis, that is, ∼1–2 mm/yr along LOS. It reinforces our initial observation that the PS positions on Envisat time-series (posterior to 2003) do not reveal any significant transient pattern.

3.4 PS mean velocity fields for the western zone (from lon. 33°30' to 34°55')

Contrary to the previous frame, the adjacent frame to the west (Fig. 1) covers a segment of the NAFZ where the role of the southern fault system is expected to be minor. Moreover, no earthquake with magnitude higher than 5 has occurred in this area during the ERS and Envisat missions. We present the PS-velocity fields deduced from two dense radar images time-series from Envisat acquisitions: first in descending pass, then in ascending pass (see image footprints in Fig. 1).

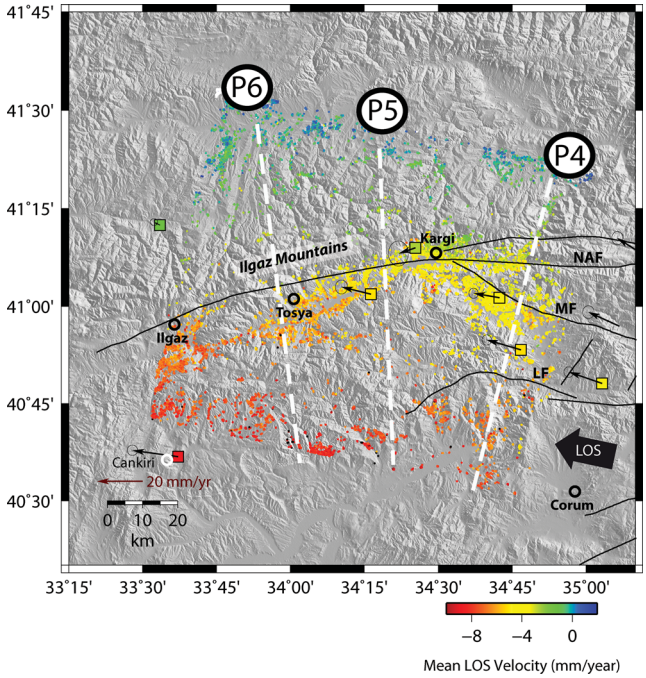

Figure 5. PS mean velocity map from Envisat archives in descending orbits on the western frame. GPS velocity field with 95 per cent confidence ellipses is from Yavasoglu *et al.* (2011). Coloured squares at GPS sites represent the GPS velocities projected onto the satellite LOS. Profiles shown in Fig. 6 are plotted with dashed white lines.

The PS mean velocity map obtained from Envisat descending acquisitions (track 436) is presented on Fig. 5. The image time-series consists of 48 acquisitions from 2003 December to 2010 September (Fig. A3). This time-series has been processed with a threshold of random false-PS percent (PR) equal to 5 per cent. Despite such a heavy constraint, 35 748 PS have been detected. Their spatial density ranges from no more than ∼5 PS/km^2 in the mountainous areas, to ∼20 PS/km^2 in the vicinity of the NAF and MF.

As indicated by the superposition of the GPS velocities projected along the satellite LOS on the PS mean velocity field (Fig. 5), the agreement between them is excellent. The RMS of the difference between the deviations of these two data sets relative to their own best fit plane is 1.1 mm/yr (Fig. A7a). The pattern of ground deformation is clearly centred along the trace of the NAF, and the relative motion of the 2 blocks estimated to 8 ± 1 mm/yr in LOS (23 ± 2–3 mm/yr in horizontal direction parallel to the fault). This slight, but significant, increase with respect to the eastern frame can simply be explained by some of the fault slip on the eastern track being accommodated by the Lacin Fault south of the main NAF trace.

Profile P4 shown in Figs 5 and 6 indicates ∼6 mm/yr of gradual LOS velocity change centred on the main NAF trace. About 80 per cent of this deformation is accommodated within a strip of 30 ± 10 km width (between 55 and 85 km). Despite the low density of PS over the hilly landscape cut by the LF, ∼1 mm/yr of LOS seems to be accommodated between LF and MF (between 40 and 50 km), while, as already noted, ∼1 mm/yr of additional LOS deformation appears to be accommodated in the vicinity of the Lacin fault zone (between 25 and 45 km).

Further west, ∼10 km west of the junction of the main NAF branches, profile P5 is oriented ∼N5W° (Figs 5 and 6). Similarly to the profile P3 of the eastern track, it clearly highlights a gradient of LOS deformation of ∼6 mm/yr centred on the NAFZ and accommodated within 30 ± 10 km (between 50 and 80 km). Despite the low density of PS north of the NAFZ, the apparent symmetry of this gradient relative to the NAF surface trace does not plead for the possible asymmetry suggested by profile P3 in this same area. To the south, the density of PS is unfortunately very low to be definitive about its interpretation. Nevertheless, ∼1 mm/yr of LOS velocity change is found again close to the LF (between 5 and 15 km).

Finally, on the eastern side of the track (profile P6 in Figs 5 and 6), ∼8 mm/yr of relative LOS deformation is found. 80 per cent of this far-field rate is accommodated within 20 ± 10 km (between 40 and 60 km). This deformation is centred on the NAF trace, but the low density of PS within the Ilgaz Mountains and their high disparity make their interpretation rather uncertain north of the NAF.

The ERS satellite also imaged this western descending track. Because our previous analysis (paragraph 3.3) indicates that no significant post-seismic deformation from the 1999 Izmit/Düzce events affects the tectonic loading of this central part of the NAFZ, we processed the whole ERS archive, including acquisitions after the Izmit and Düzce earthquakes (Fig. A4). This time-series is much less dense than the Envisat time-series (only 24 images), leading to a noisier PS mean velocity field. However, the results are globally similar to those presented before (Fig. A9): the location, the shape and the amplitude of the deformation are the same. Most of it is centred on the NAF while ∼1 mm/yr of LOS deformation seems to be accommodated by the LF.

This western zone is also imaged by the ERS and Envisat satellites in ascending orbits (Fig. 1). Since the ERS archives are very sparse, we present here the PS mean-velocity field from a 15 Envisat images (track 28, frame 816) time-series spanning the 2004–2010 period (Fig. A5). Once again, the PR threshold is set to 5 per cent, leading to the selection of 14 216 PS (up to ∼10 PS/km^2 in the flat areas close to the MF and the NAFZ, and below ∼3 PS/km^2 over the hilly landscapes). Because a PS in ascending orbit generally differs from a PS in descending orbit, the spatial distribution of PS significantly changes from the previous analysis in descending orbit.

The PS mean velocity field for Envisat ascending orbits is presented in Fig. 7. For this image, the motion of the Anatolian block (relative to Eurasia) is positive with respect to the satellite located to the west. Despite the low density of the time-series, the agreement between PS and GPS projected along the LOS is still good (RMS = 1.8 mm/yr) (Fig. A7c). The deformation is centred on the NAF and appears to be quite uniform laterally. The faint velocity gradient that was detected in descending orbits close to the Lacin fault is still visible here in the south-eastern part of the scene.

The profile P7 (Figs 7 and 8) has a N5W° orientation and is located on the eastern side of the track. It indicates a velocity change of 6 ± 1 mm/yr in LOS clearly centred on the NAF surface trace. 80 per cent of this deformation is accommodated within a ∼20 ± 5 km-wide strip, in a classic interseismic arctangent shape (between 45 and 65 km). Further south, a clear velocity offset of ∼2 mm/yr is mapped across the LF. This confirms the active tectonic loading of the LF already evidenced by the PSI analysis of the radar archives acquired in descending pass. Furthermore, the slight increase of this velocity offset relative to its estimation in descending pass, suggests that this velocity change on the ground is now more collinear to the LOS, which complies with the strike of this western extremity of the LF.

The shape of the velocity changes along the profile P8, located ∼30 km to the west, is similar to the one observed along the profile P7. Despite a lower PS density, a velocity gradient of ∼6 mm/yr is observed across the NAFZ (most of which is accommodated

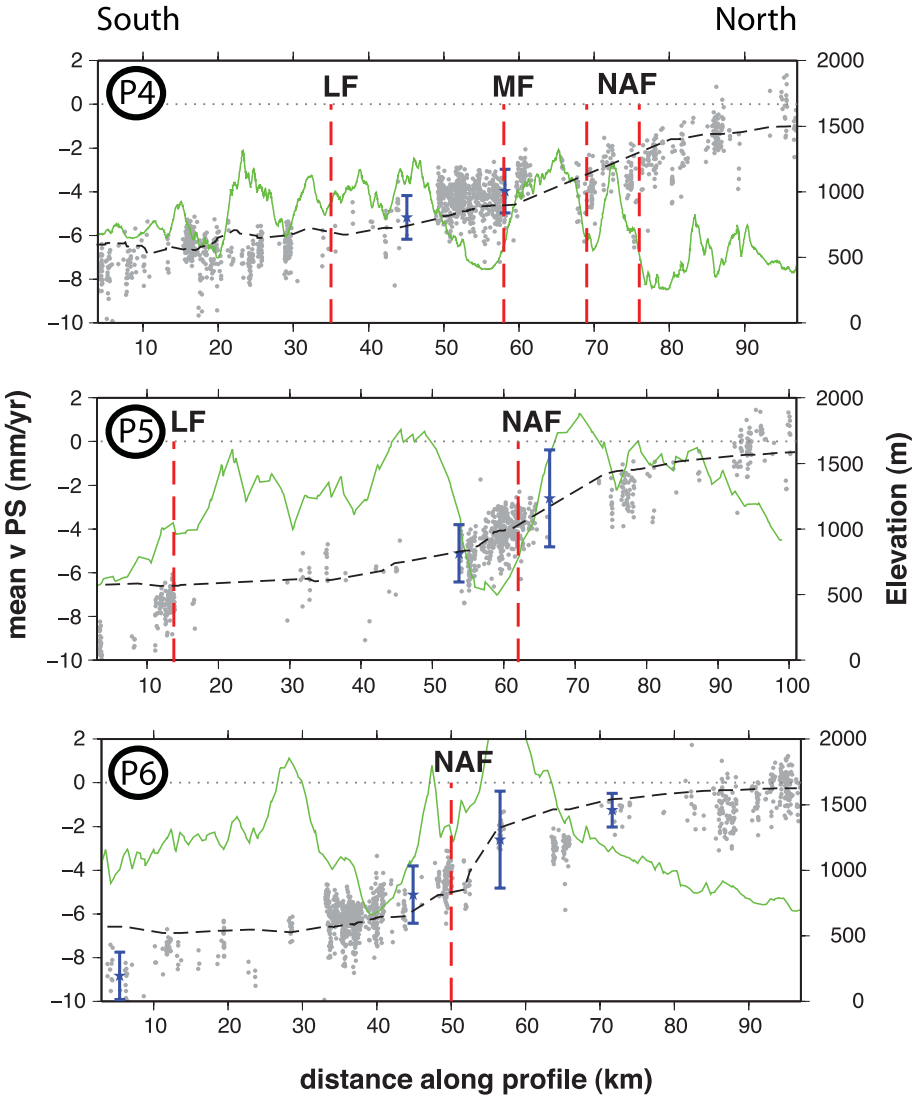

Figure 6. Comparison of GPS velocities along the satellite LOS (blue stars with error bars) and PS mean velocities (grey circles) for the three profiles whose locations are shown in Fig. 5. PS are selected within a ± 3 km distance from the profile. GPS are selected within a ± 10 km distance from the profile for profiles P4 and P5, ± 30 km for P6. The locations of the faults along the profiles are indicated with red vertical dashed lines. Topography along the profile is shown in green curve. The black dotted line indicates the LOS velocity profile predicted by our slip-rate model at depth described in paragraph 4. Abbreviations as in Fig. 1.

between 40 and 60 km), while ∼1 mm/yr of LOS deformation is still likely accommodated by the LF.

Finally, ∼20 km further west, the profile P9 shows ∼6 mm/yr of LOS velocity change across the NAF. 80 per cent of this deformation is accommodated within 20 ± 10 km (between 40 and 60 km). No additional deformation is detected in the southern part of this imaged zone. The deformation accommodated by the LF more to the east, is now probably transferred more to the south. Further west, the spatial density of PS becomes too low to be reliably interpreted.

The global agreement between PS and GPS measurements along this central bend of the NAF suggests that the vertical component of the deformation is negligible. In order to check it out, we combine these two PS mean velocity fields obtained in ascending and descending passes over the western frame for estimating the 3-D components of the ground deformation. This procedure requires the addition of a third independent measurement of the ground deformation. In the case of coseismic deformation, one usually complements the InSAR displacement fields with the spatially dense horizontal displacement fields deduced from the subpixel correlation of a pair of radar or optical images spanning the earthquake (e.g. Fialko *et al.* 2001, 2005). Here, we simply interpolate the horizontal GPS velocity field all over the scene and use its azimuth as an additional constraint for the estimation of the 3D velocity vector (e.g. Peyret *et al.* 2011).

The 3-D velocity field deduced from this combination of PS-velocity fields and horizontal GPS azimuth is shown in Fig. A10. Despite the high uncertainty associated with the interpolated GPS velocity field (mainly due to the low spatial density of the GPS network), the mean vertical velocity all over this area is estimated to ∼0.4 mm/yr with an RMS ∼0.7 mm/yr. The only localized pattern of significant subsidence (∼4 mm/yr) appears in the eastern part of the scene, close to the city of Ilgaz. But, in this area, we consider that the density of PS in ascending pass is too low to be reliable. Hence, we conclude that, over this western frame, no significant vertical motion can be inferred from our PS analysis.

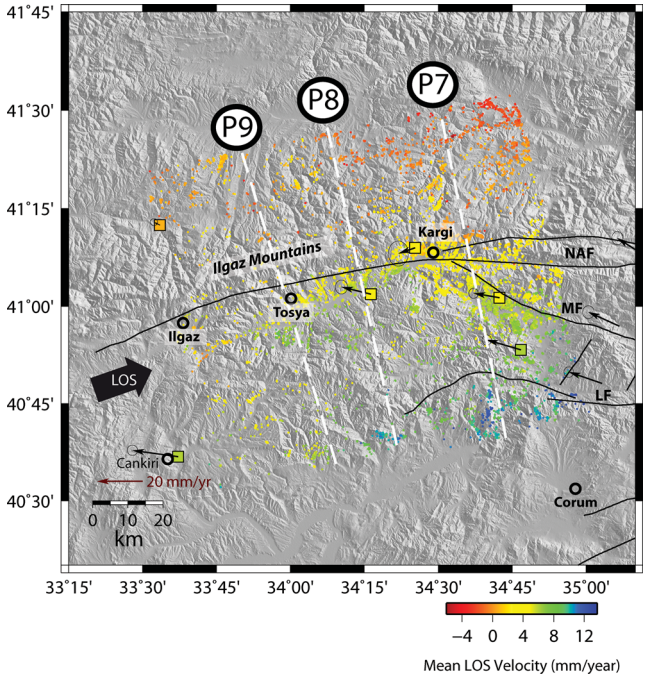

Figure 7. PS mean velocity map from Envisat archives in ascending orbits on the western frame. GPS velocity field with 95 per cent confidence ellipses is from Yavasoglu *et al.* (2011). Coloured squares at GPS sites represent the GPS velocities projected onto the satellite LOS. Profiles shown in Fig. 8 are plotted with dashed white lines.

4 SLIP MODEL AT DEPTH

The PS- and GPS-velocity fields described above are the surface expression of deformation at depth. A large class of models has been proposed among which we cite two major end members: a purely kinematic model of elastic block motion (e.g. Meade & Hager 1999; McCaffrey 2002), and a mechanical model of continuous deformation (e.g. Chéry *et al.* 2011). This latter approach may appear well adapted to the wide spatial distribution of fault segments between the NAFZ to the north and the Sungurlu fault (SF) system to the south. However, it does not permit estimation of the slip-rate or slip-rate deficit distribution on faults, and generally requires prior information about rheology that we do not have in the study area. Accordingly, in this paper, we adopt the elastic-block framework. In this approach, the study area is decomposed into blocks separated by faults. Consequently, the velocity field is decomposed into a long-term component due to relative block rotation, and an interseismic slip-rate deficit distribution on the faults (e.g. Savage & Burford 1973).

For estimating the interseismic slip-rate distribution along this central segment of the NAFZ from our dense PS data sets, we carry out a two-step inversion scheme. First, we adopt a block segmentation of this central NAFZ area similar to the one proposed by Yavasoglu *et al.* (2011). Then, using the 'defnode' software (McCaffrey 1995), we estimate the relative block rotations from the GPS velocity field of Yavasoglu *et al.* (2011) that we complement to the east with the GPS velocity field of Tatar *et al.* (2012). This calculation also provides a rough estimate (due to the low spatial density of the GPS velocity field) of the slip-rate deficit distribution on the faults. In order to obtain a finer model of coupling along the fault from our PSI results, and considering the excellent agreement between PS velocity fields and GPS, we subtract the predicted long-term velocity field from our PS-velocity fields. Finally, we interpret these PS-velocity fields, corrected from block rotations, in terms of the distribution of back-slip along fault segments. This can be solved as a dislocation imbedded in an elastic half-space. Therefore, we use a regularized weighted least-square inversion scheme (e.g. Du *et al.* 1992; Peyret *et al.* 2008) for inverting the PS-velocity fields. This procedure involves inversion of matrices whose dimensions are the number of slip parameters to estimate (a few tens), and the number of geodetic measurements (a few thousands for PS). Therefore we subsample the PS-velocity field by applying a threshold on disparity so as to reduce their density to about 5000 PS per track.

The segmentation of this area into only two blocks (Eurasia and Anatolia) leads to a model (combination of block rotations and back-slip on faults) that does not satisfactory predict the GPS velocity field in the eastern corner of the wedge comprised between the NAF and the SF systems (Fig. A11). This suggests that this wedge should be treated as an additional block. This assumption is supported by a palaeomagnetic analysis (Isseven & Tüysüz 2006) that reveals predominant clockwise rotation of the area between the NAF and the SF, as expected for a block (or a set of blocks) delimited by dextral faults. Consequently, between the Eurasian and Anatolian blocks, we define a third block delimited by the main NAF branch to the north, the SF to the south, and the Dodurga fault zone to the west (Fig. 1). We model the NAF and SF as vertical faults.

With such a geometrical model, the inversion of the GPS velocity fields leads to a rotation of the central block relative to Eurasia of 1.9 deg/Myr counter-clockwise around a pole located at (N36°23', E33°44').This Euler pole is slightly different from the one of the Anatolian block (e.g. Reilinger *et al.* 2006). This model predicts quasi-uniform long-term slip-rates along the NAF and the SF of ∼20 mm/yr and ∼5 mm/yr, respectively, and a locking depth of ∼15 km on the NAF (Fig. A11). However, this model has a necessarily low resolution at depth (even sometimes at shallow depths) due to the poor spatial density of GPS measurements. Hence, we now subtract this predicted long-term motion from the PS mean velocity fields and invert these high spatial resolution data sets in terms of slip-rate deficit on the NAF and SF. Since the relative contribution of the SF is small, we will only present the results of our inversion on the NAF.

Thanks to the high density of PS, we can solve for back-slip distribution along a highly discretized fault geometry. We decompose the NAF fault into 20 segments ∼18 km-long along strike, and 10 segments along dip whose width increases geometrically from 0.5 km at the surface up to 20 km at 60 km depth. The increasing size of the patches roughly counterbalances the decrease of the model resolution with depth (e.g. Fialko 2004) (Fig. 9b). The resolution of the model presented in this paper is high very close to the surface in the central part of the study zone where the density of PS close to the NAF is high. By contrast, west of longitude ∼34° this density of PS in the near-field becomes very low leading to a very poor resolution close to the surface. The resolution is very low on the western extremity of the NAF that is outside the area covered by the GPS and PS velocity fields. Therefore, it will be trimmed in the subsequent figures. The contribution of the PS velocity fields to the increase of the model resolution obtained with only GPS is illustrated on Fig. A12. Its improvement is particularly notable between longitude 33°50' and 35°10' where the PS density is high both in the near- and far-field.

Without any regularization constraint, the standard least-square inversion generally leads to slip models with unrealistic slip changes from one patch to its neighbours. Therefore, we impose the constraint that the roughness of the slip-rate model (the finite difference approximation of its Laplacian) must be sufficiently small. The

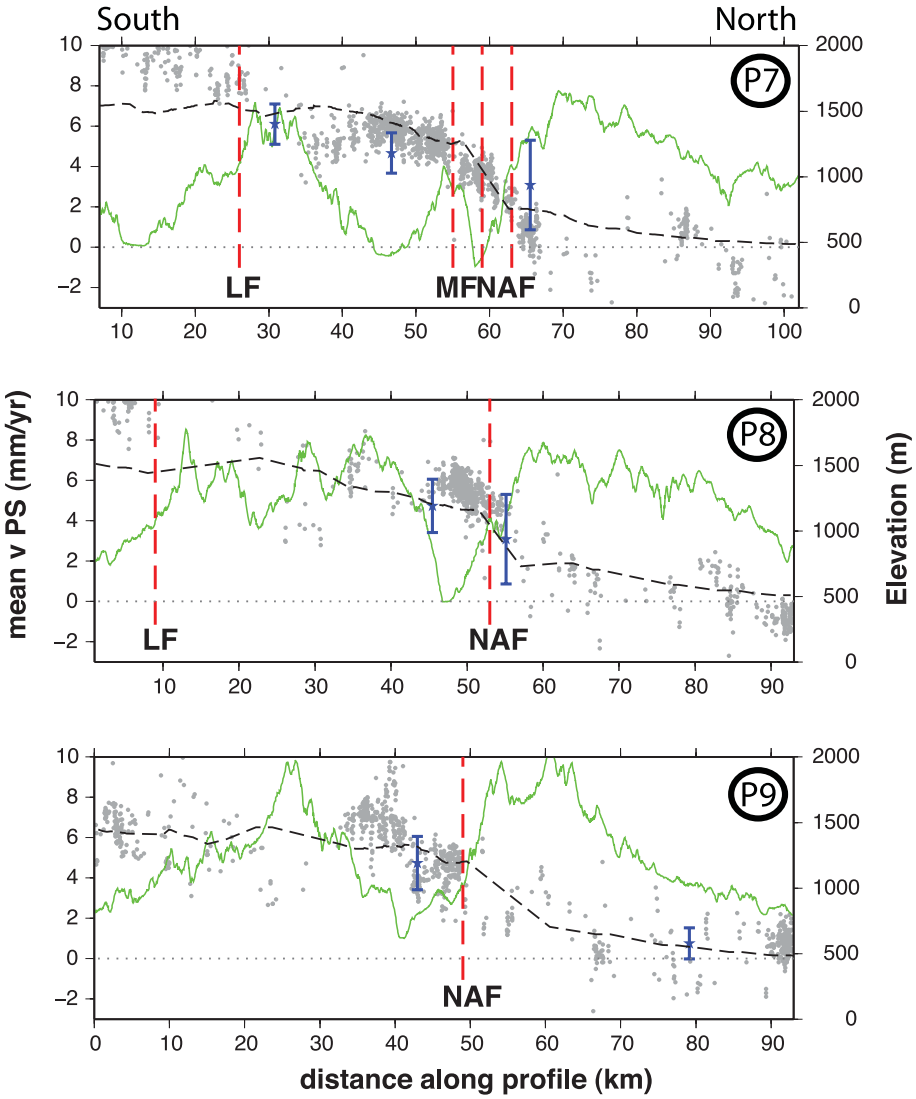

Figure 8. Comparison of GPS velocities along the satellite LOS (blue stars with error bars) and PS mean velocities (grey circles) for the three profiles whose locations are shown in Fig. 7. PS are selected within a ± 3 km distance from the profile. GPS are selected within a ± 20 km distance from the profile. The locations of the faults along the profiles are indicated with red vertical dashed lines. Topography along the profile is shown in green curve. The black dotted line indicates the LOS velocity profile predicted by our slip-rate model at depth described in paragraph 4. Abbreviations as in Fig. 1.

relative influence of this constraint is chosen so as to obtain a slip-rate distribution roughly ranging from 0 (creeping at depth), to 20 ± 5 mm/yr (back-slip completely counterbalancing the long-term slip for the locked part of the fault).

Our preferred model of back-slip distribution is presented on Fig. 9a. It predicts fairly well all the GPS and PS velocity fields, leading to mean residues between measured and predicted data of 2 mm/yr (RMS = 1.5 mm/yr), −0.1 mm/yr (RMS = 1.5 mm/yr), −0.4 mm/yr (RMS = 1.4 mm/yr) and 0.2 mm/yr (RMS = 1.9 mm/yr) for the GPS, the descending Envisat on the eastern frame, the descending Envisat on the western frame and the ascending Envisat on the western frame data sets, respectively (Fig. A13). This good agreement is also illustrated on Figs 3, 6 and 8 with the superposition of the predicted LOS velocities on the GPS- and PS-LOS velocity profiles. However, two significant discrepancies between the modelled and the measured velocity fields are found: along the very close proximity of the NAF and south of the LF. The former discrepancy may be explained both by the limited spatial resolution of the slip-rate model close to the surface, and the relative imprecision of the geometrical model adopted for the NAF. More significant is the latter discrepancy. It shows that our simple slip-rate model limited to the NAF fails to predict this southern deformation which is probably fully accommodated by the LF. The mean locking depth (slip-rate deficit lower than ∼5 mm/yr) is estimated to ∼20 km, which complies, within the uncertainties, with the elastic block modelling from GPS. This locking depth appears to be rather constant all along this central bend of the NAF. However, our model suggests a possible slight change along strike. Close to the centre of this central bend (longitude ∼E34°50') and eastwards, the locking depth of the NAF is estimated between 15 and 20 km. It appears to be significantly shallower than for the western section (between longitudes E34°20' and E34°50'), for which the locking depth is estimated between 25 and 30 km. Finally, at the western end of our model, the upper limit of the deep creeping zone rises again to ∼15–20 km (between longitudes E34°20' and E33°40'). Moreover, the predicted back-slip on the shallower part of this segment (between longitudes E33°40' and E34°20') does not fully compensate the predicted long-term slip, thus suggesting

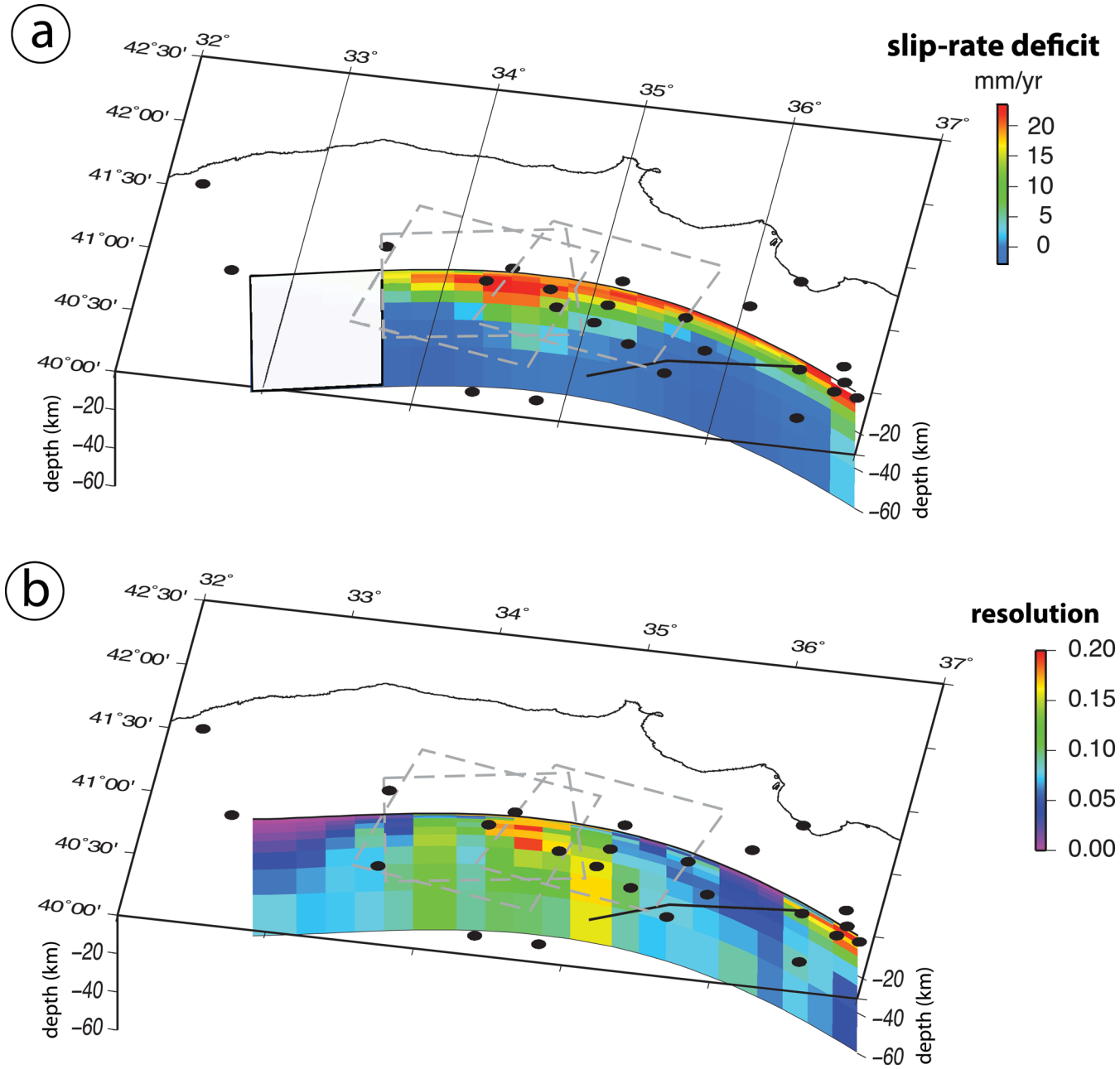

Figure 9. (a) Model of slip-rate deficit distribution along the simplified NAF fault from the inversion of the PS-mean velocity fields. Black dots indicate the location of the GPS sites. (b) Resolution of the model.

some slight creeping at the surface (∼5 mm/yr) from the model. Nevertheless, this interpretation must be toned down, if not ruled out, by the low resolution of the model in this upper part of the fault, due to the lack of measurements in the near field of the NAF. Indeed, field observations do not report any surface creep in this area. Extending our analysis more to the west could investigate whether this westward-locking depth decrease is going on towards the Ismetpasa creeping zone whose eastern end is located ∼30 km further west (Cakir *et al.* 2005).

5 DISCUSSION

Three major arguments support the reliability of the PS-velocity fields presented in this study. First, we processed the ERS and Envisat independent data sets on both descending tracks, and all of them led to PS velocity fields with the same patterns. Moreover, if we reduce even more the PR threshold, the PS reliability increases (at the cost of spatial density), but the main features remain similar. Finally, whatever frame and radar time-series we consider, the agreement between GPS and PS mean velocity is very good (RMS ∼1 mm/yr).

The good agreement between GPS and PS velocities suggests that no significant (typically ∼2 mm/yr) vertical deformation affects the study area. This is confirmed by the 3D velocity field inferred from the PS velocity fields obtained in ascending and descending pass on the western track. Its vertical component is estimated to be lower than 1 mm/yr. We detected only one small zone of possible uplift (Fig. 2 and profile P2 on Fig. 3). It could be related to its

particular location between two fault segments with south–north orientations. Nevertheless, even though no significant PS-velocity pattern correlated with the topography has been found elsewhere on the study area, one cannot rule out an atmospheric residue as a possible explanation of this pattern. So, this apparent uplift requires additional evidence to be well defined. Furthermore, our PS analyses indicate that the mean velocity fields do not change significantly between the periods spanned by the ERS and the Envisat acquisitions. However, because the Envisat time-series starts more than 3 yr after the Izmit and Düzce earthquakes, our analysis cannot constrain possible short-term post-seismic deformation from these events.

Contrary to some other fault systems where a pronounced asymmetry in strain accumulation has been found (e.g. Fialko 2006), none of our PS-velocity maps exhibit any clear asymmetry across the NAF. We could suspect some asymmetry on profile P3, but we did not find any clear confirmation of that neither from the processing of the ERS time-series (too high uncertainties), nor from the nearby profile P5. So, this first-order symmetry is in agreement with the geological context that indicates that, in this central bend, the NAFZ is entirely confined to the Tethyside accretionary material (Sengör *et al.* 2004). Moreover, this is consistent with a dip angle of the NAF that would not significantly differ from the vertical, even at depth. Finally, it complies with the lack of deformation apparently accommodated by the MF or any other subparallel fault segment in the vicinity of the NAF. Indeed, ∼1–2 mm/yr of additional LOS strain accumulation has been detected south of the NAF but only ∼30 km to the south, along the LF.

Our analysis provides new information on the present-day activity of the southern fault system. First, the Salhan Çayi event clearly struck one branch of the Lacin Fault. Second, the interseismic PS velocity fields show that ∼1–2 mm/yr along the LOS is probably accommodated across the Lacin Fault. Therefore, the role of this southern fault system, and more specifically the LF, will have to be taken into account for any comparison between the geodetically and geologically determined fault slip rates on this segment of the NAF.

Since we expect the locked zones to be prone to seismic failure contrary to creeping zone at depth, we compare our model to the earthquake distribution from the centennial earthquake catalogue (CEC) (Engdahl & Villaseñor 2002), the USGS catalogue, and the set of relocated earthquakes from Yolsal-Cevikbilen *et al.* (2012) (Fig. 10). The location of the events from the USGS catalogue may be rather imprecise. Nevertheless, the deeper events located between longitudes E34°15' and E34°45' occur along the section where our model predicts a deeper locking depth. Overall, the global agreement between our model results and these catalogues of seismicity is reasonable. However, more dense, precise, and complete catalogues of seismicity are required for a more detailed comparison.

6 CONCLUSIONS

The application of the PSI technique provides coherent and demonstrably reliable crustal deformation estimates in a region of Anatolia characterized by dense forests north of the NAF, and extensive agricultural activities south of the NAF. We obtained precise and high spatial resolution maps of the ground deformation induced by tectonic loading on the central bend of the NAF. Deformation is related both to the coseismic displacement due to the moderate Salhan Çayi earthquake and to the interseismic deformation that we show to be steady over the time intervals spanned by the ERS and Envisat acquisitions (prior and 3 yr after the major Izmit and Düzce earthquakes). Our analysis demonstrates that Envisat time-series, as well as the GPS velocity field (measured between 2001 and 2005) are free of any significant transient post-seismic deformation. Despite the scalar nature of LOS measurements, they are in excellent agreement with the horizontal GPS velocity field published for this area. Even though it does not prove the robustness of the whole PS velocity fields, it shows the compatibility of PS and GPS velocity fields at the GPS network spatial scale (a few tens of kilometres). Yet, this agreement suggests that no significant vertical deformation occurs along this segment of the NAF at large spatial scales, in spite of the apparent restraining bend geometry of this segment. This is confirmed by the estimation of the 3-D ground velocity field from the combination of the PS mean velocity fields in ascending and descending pass, with the horizontal GPS velocity field. We identify only one small area that appears to be uplifting between two fault systems oriented approximately perpendicularly to the general east-west trend of the NAFZ. In addition, the PS velocity maps and profiles indicate that tectonic loading is almost totally accommodated by the NAF, while the southern LF system accommodates ∼2–3 mm/yr if pure right-lateral strike-slip is assumed (∼ 1 mm/yr in LOS).

The high spatial density of PS also permits us to estimate a model of slip-rate deficit along the faults with a much higher spatial resolution than is usually obtained from GPS networks. Thus, our inversion leads to a model whose slip-rate of ∼20 mm/yr is rather uniform, but whose locking depth varies laterally between ∼15 km and ∼25 km. These variations seem to be fairly well correlated with the seismicity distribution, although the depths of most seismic events are poorly constrained. Obtaining such precise models of slip distribution at depth is fundamental for seismic hazard analyses. In the light of our model, it would be informative to get additional measurements of the velocity gradients across the NAF with dense GPS profiles, particularly in the western part of our study zone.

Our study demonstrates that, even over such a vegetated area, the PSI analysis of C-Band radar acquisitions is able to provide dense and precise mapping of the interseismic deformation. This analysis could be easily extended to the whole NAF length (e.g.

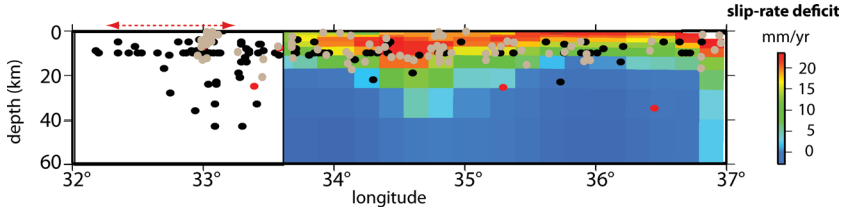

Figure 10. Seismicity at the vicinity of the NAFZ from the centennial earthquake catalogue (Engdahl & Villaseñor 2002), the USGS catalogue (http://earthquake.usgs.gov/earthquakes/eqarchives/epic/) and the list of relocated earthquakes from Yolsal-Cevikbilen *et al.* (2012), in red, black and grey circles respectively, superimposed on our model of slip-rate deficit distribution along the NAF fault. The red dotted arrow indicates the spatial extension of the Ismetpasa creep segment of the NAF (Cakir *et al.* 2005).

Motagh *et al.* 2007b) and thus provide a complete detailed view of the lateral changes of the strain distribution across the fault. These results might be compared with the one obtained from ALOS data analyses, either with a PSI approach or by a simple stacking interferograms (e.g. Fialko *et al.* 2011). As illustrated in this paper, these new spatially and temporally dense InSAR measurements will significantly improve our understanding of the lateral variations of the mechanical behaviour of the lithosphere all along the NAFZ.

ACKNOWLEDGMENTS

All Envisat SAR data were provided and copyrighted by the European Space Agency. We are grateful to A. Hooper for use of 'Stamps' software, and JPL/Caltech for use of the ROI_PAC software. The interferometric processing was performed using the freely available Doris software package developed by the Delft Institute of Earth Observation and Space Systems (DEOS), Delft University of Technology. All figures were drawn using the Generic Mapping Tools (Wessel & Smith 1998). This research was supported in part by the CNRS 'Télédétection Spatiale', 'Catastrophes Naturelles' and 'Mistral' programs, and NSF-EAR grant 0838488 to MIT. We thank T. Wright and one anonymous reviewer for their very constructive comments that improved this manuscript greatly.

REFERENCES

Adam, N., Kampes, B. & Eineder, M., 2004. The development of a scientific Permanent Scatterer system: modifications for mixed ERS/Envisat time series, in *Proceedings of the 2004 Envisat & ERS Symposium,* Salzburg, ESA SP-572, April 2005.

Aktug, B. *et al.*, 2009. Deformation of western Turkey from a combination of permanent and campaign GPS data: limits to block-like behaviour, *J. Geophys. Res.,* **114,** B10404.

Ambraseys, N.N., 1970. Some characteristics of the North Anatolian Fault Zone, *Tectonophysics,* **9,** 143–165.

Ambraseys, N.N., 2009. *Earthquakes in the Eastern Mediterranean and Middle East: A Multidisciplinary Study of Seismicity up to 1900,* Cambridge University Press, New York, pp. 512–515.

Armijo, R., Meyer, B., Hubert, A. & Barka, A, 1999. Westward propagation of the North Anatolian fault into the northern Aegean: timing and kinematics, *Geology,* **27,** 267–270.

Barka, A., 1992. The North Anatolian fault zone, *Ann. Tectonicae (Special Issue),* **6,** 164–195.

Barka, A., 1996. Slip distribution along the North Anatolian fault associated with large earthquakes of the period 1939 to 1967, *Bull. Seismol. Soc. Am.,* **86,** 1238–1254.

Barka, A., Akyüz, H.S., Cohen, H.A. & Watchorn, F., 2000. Tectonic evolution of the Niksar and Tasova-Erbaa pull-apart basins, North Anatolian Fault Zone: their significance for the motion of the Anatolain block, *Tectonophysics,* **322,** 243–264.

Bergougnan, H., 1975. Relations entre les édifices pontiques et tauriques dans le nord-est de l'Anatolie, *Bull. Soc. Geol. Fr.,* **17,** 763–773.

Bernardino, P., Fornaro, G., Lanari, R. & Sansosti, E., 2002. A new algorithm for surface deformation monitoring based on small baseline differential SAR interferograms, *IEEE Trans. Geosci. Remote Sens.,* **40**(11), 2375–2383.

Biggs, J., Bergman, E., Emmerson, B., Funning, G.J., Jackson, J., Parsons, B. & Wright, T.J., 2006. Fault identification for buried strike-slip earthquakes using InSAR: the 1994 and 2004 Al Hoceima, Morocco earthquakes, *Geophys. J. Int.,* **166,** 1347–1362.

Bürgmann, R., Rosen, P.A. & Fielding, E.J., 2000. Synthetic Aperture Radar Interferometry to measure Earth's surface topography and its deformation, *Ann. Rev. Earth Planet. Sci.,* **28,** 169–209.

Cakir, Z., Akoglu, A.M., Belabbes, S., Ergintav, S. & Meghraoui, M., 2005. Creeping along the Ismetpasa section of the North Anatolian fault (Western Turkey); rate and extend from InSAR, *Earth Planet. Sci. Lett.,* **238,** 225–234.

Chéry, J., Mohammadi, B., Peyret, M. & Joulain, C., 2011. Plate Rigidity Inversion in Southern California using interseismic GPS Velocity Field, *Geophys. J. Int.,* **187**(2), 783–796.

Delouis, B., Giardini, D., Lundgren, P. & Salichon, J., 2002. Joint inversion of InSAR, GPS, teleseismic, and strong-motion data for the spatial and temporal distribution of earthquake slip: application to the 1999 Izmit mainshock, *Bull. Seismol. Soc. Am.,* **92,** 278–299.

Du, Y., Aydin, A. & Segall, P., 1992. Comparison of various inversion techniques as applied to the determination of a geophysical deformation model for the 1983 Borah Peak earthquake, *Bull Seism. Soc. Am.,* **82,** 1840–1866.

Emardson, T.R., Simons, M. & Webb, F.H., 2003. Neutral atmospheric delay in interferometric synthetic aperture radar applications: statistical description and mitigation, *J. Geophys. Res.,* **108**(B5), 2231.

Engdahl, E.R. & Villaseñor, A., 2002. Global seismicity: 1900–1999, in *International Handbook of Earthquake and Engineering Seismology, Part A, Chapter 41,* pp. 665–690, eds Lee, W.H.K., Kanamori, H., Jennings, P.C. & Kisslinger, C., Academic Press, Boston.

Ergintav, S., Bürgmann, R., McClusky, S., Cakmak, R., Reilinger, R.E., Lenk, O., Barka, A. & Özener, H., 2002. Postseismic deformation near the Izmit earthquake (08/17/99, M = 7.5) rupture zone, *Bull. Seismol. Soc. Am.,* **92,** 194–207.

Ergintav, S. *et al.*, 2009. Seven years of postseismic deformation following the 1999, M = 7.4 and M = 7.2, Izmit-Düzce, Turkey earthquake sequence, *J. Geophys. Res.,* **114,** B07403.

Farr, T.G. *et al.*, 2007. The Shuttle Radar Topography Mission, *Rev. Geophys.,* **45,** RG2004.

Ferretti, A., Prati, C. & Rocca, F., 1999. Permanent scatterers in SAR interferometry, in *International Geoscience and Remote Sensing Symposium,* Hamburg, Germany, pp. 1–3.

Ferretti, A., Prati, C. & Rocca, F., 2001. Permanent scatterers in SAR interferometry, *IEEE Trans. Geosci. Remote Sens.,* **39**(1), 8–20.

Fialko, Y., 2004. Probing the mechanical properties of seismically active crust with space geodesy: study of the coseismic deformation due to the 1992 M_w 7.3 Landers (southern California) earthquake, *J. Geophys. Res.,* **109,** B03307.

Fialko, Y., 2006. Interseismic strain accumulation and the earthquake potential on the southern San Andreas fault system, *Nature,* **441,** doi:10.1038/nature04797.

Fialko, Y., Simons, M. & Agnew, D., 2001. The complete (3-D) surface displacement field in the epicentral area of the 1999 M_w 7.1 Hector Mine earthquake, California, from space geodetic observations, *Geophys. Res. Lett.,* **28**(16), 3063–3066.

Fialko, Y., Sandwell, D., Simons, M. & Rosen, P., 2005. Three-dimensional deformation caused by the Bam, Iran, earthquake and the origin of shallow slip deficit, *Nature,* **435,** doi:10.1038/nature03425.

Fialko, Y., Kaneko, Y., Tong, X., Sandwell, D.T. & Furuya, M., 2011. Investigation of interseismic deformation along the central section of the North Anatolian fault (Turkey) using InSAR observations and earthquake-cycle simulations, *AGU fall meeting 2011*, T31E-08.

Hartleb, R.D., Dolan, J.F., Akyüz, H.S. & Yerli, B., 2003. A 2000-year-long paleoseismologic record of earthquakes along the Central North Anatolian Fault, from trenches at Alayurt, Turkey, *Bull. Seism. Soc. Am.,* **93**(5), 1935–1954.

Hearn, E.H., Hager, B.H. & Reilinger, R.E., 2002. Viscoelastic deformation from North Anatolian Fault Zone earthquakes and the eastern Mediterranean GPS velocity field, *Geophys. Res. Lett.,* **29**(11), 1549.

Hearn, E.H., McClusky, S., Ergintav, S. & Reilinger, R.E., 2009. Izmit Earthquake postseismic deformation and dynamics of the North Anatolian fault zone, *J. Geophys. Res.,* **114,** B08405.

Hooper, A.J., 2006. Persistent scatterer radar interferometry for crustal deformation studies and modelling of volcanic deformation, *PhD thesis,* Stanford University.

Hooper, A., Zebker, H., Segall, P. & Kampes, B., 2004. A new method for measuring ground deformation on volcanoes and other natural

terrains using InSAR persistent scatterers, *Geophys. Res. Lett.,* **31**(23), L23611.

Hooper, A., Segall, P. & Zebker, H., 2007. Persistent scatterers InSAR for crustal deformation analysis, with application to Volcan Alcedo, Galapagos, *J. Geophys. Res.,* **112,** B07407.

Hubert-Ferrari, A., Armijo, R., King, G., Meyer, B. & Barka, A.A., 2002. Morphology, displacement, and slip rates along the North Anatolian fault, Turkey, *J. Geophys. Res.,* **107,** 2235.

Isseven, T. & Tüysüz, O., 2006. Palaeomagnetically defined rotations of fault-bounded continental blocks in the North Anatolian Shear Zone, North Central Anatolia, *J. Asian Earth Sci.,* **28,** 469–479.

Kahle, H. -G., Concord, M., Peter, Y., Geiger, A., Reilinger, R., Barka, A. & Veis, G., 2000. GPS derived strain rate field within the boundary zones of the Eurasian, African, and Arabian plates, *J. Geophys. Res.,* **105,** 23 353–23 370.

Kampes, B.M., 2005. Displacement parameter estimation using permanent scatterer interferometry, *PhD thesis,* Delft University of Technology.

Kampes, B.M., Hanssen, R.F. & Perski, Z., 2003. Radar interferometry with public domain tools, in *Third International Workshop on ERS SAR Interferometry, 'FRINGE03',* Frascati, Italy, 1–5 Dec 2003, 6.

Kozaci, O., Dolan, J., Finkel, R. & Hartleb, R., 2007. Late Holocene slip rate for the North Anatolian fault, Turkey, from cosmogenic ^{36}Cl geochronology: implications for the constancy of fault loading and strain release rates, *Geology,* **35**(10), 867–870.

Kutoglu, H.S., Akcin, H., Kemaldere, H. & Gormus, K.S., 2008. Triggered creep rate on the Ismetpasa segment of the North Anatolian Fault, *Nat. Hazards Earth Syst. Sci.,* **8,** 1369–1373.

Lohman, R.B. & Simons, M., 2005. Locations of selected small earthquakes in the Zagros mountains, *Geochem. Geophys. Geosyst.,* **6,** Q03001.

Lyons, S. & Sandwell, D., 2003. Fault creep along the southern San Andreas from interferometric synthetic aperture radar, permanent scatterers, and stacking, *J. Geophys. Res.,* **108**(B1), 2047–2070.

Manzo, M., Fialko, Y., Casu, F., Pepe, A. & Lanari, R., 2011. A quantitative assessment of DInSAR measurements of interseismic deformation: the southern San Andreas fault case study, *Pure Appl. Geophys.,* doi:10.1007/s00024-011-0403-2.

Massonnet, D. & Feigl, K., 1998. Radar interferometry and its application to changes in the earth's surface, *Rev. Geophys.,* **36**(4), 441–500.

McCaffrey, R., 1995. DEF-NODE users guide, Rensselaer Polytechnic Institute, Troy.

McCaffrey, R., 2002. Crustal block rotations and plate coupling, in *Plate Boundary Zones,* Vol. 30, pp. 101–122, eds Stein, S. & Freymueller, J., AGU Geodynamics Series. 425pp.

McClusky, S. *et al.*, 2000. Global positioning system constraints on plate kinematics and dynamics in the eastern Mediterranean and Caucasus, *J. Geophys. Res.,* **105**(B3), 5695–5719.

McClusky, S., Reilinger, R., Mahmoud, S., Ben Sari, D. & Tealeb, A., 2003. GPS constraints on Africa (Nubia) and Arabia plate motions, *Geophys. J. Int.,* **155,** 126–138.

McKenzie, D., 1972. Active tectonics of the Mediterranean region, *Geophys. J. R. Astron. Soc.,* **30,** 109–185.

Meade, B.J. & Hager, B.H., 1999. Simultaneous inversions of geodetic and geologic data for block motions in plate boundary zones, *Eos, Trans. AGU,* Paper G51B-16.

Motagh, M., Djamour, Y., Walter, T.R., Wetzel, H.-U., Zschau, J. & Arabi, S., 2007a. Land subsidence in Mashhad Valley, northeast Iran: results from InSAR, levelling and GPS, *Geophys. J. Int.,* **168**(2), 518–526.

Motagh, M., Hoffmann, J., Kampes, B., Baes, M. & Zschau, J., 2007b. Strain accumulation across the Gazikoy-Saros segment of the North Anatolian Fault inferred from Persistent Scatterer Interferometry and GPS measurements, *Earth Planet. Sci. Lett.,* **255,** 432–444.

Peyret, M., Rolandone, F., Dominguez, S., Djamour, Y. & Meyer, B., 2008. Source model for the Mw 6.1, 31 March 2006, Chalan-Chulan Earthquake (Iran) from InSAR, *Terra Nova,* **20**(2), 126–133.

Peyret, M., Dominguez, S., Cattin, R., Champenois, J., Leroy, M. & Zajac, A., 2011. Present-day interseismic strain distribution along the Longitudinal Valley, Eastern Taiwan, from a PS-InSAR analysis of the ERS satellite archives, *J. Geophys. Res.,* **116,** B03402.

Provost, A.S., Chéry, J. & Hassani, R., 2003. 3-D mechanical modeling of the GPS velocity field along the north Anatolian fault, *Earth Planet. Sci. Lett,* **209,** 361–377.

Reilinger, R.E. *et al.*, 1997. Global Positioning System measurements of the present day crustal movements in the Arabia-Africa-Eurasia plate collision zone, *J. Geophys. Res.,* **102,** 9983–9999.

Reilinger, R. *et al.*, 2006. GPS constraints on continental deformation in the Africa-Arabia-Eurasia continental collision zone and implications for the dynamics of plate interactions, *J. Geophys. Res.,* **111,** B05411.

Rojay, B. & Koçyiğit, A., 2011. An active composite pull-apart basin within the central part of the North Anatolian fault system: Merzifon – Suluova Basin, Turkey, *Turkish J. Earth Sci.,* **21,** 473–496.

Rosen, P.A., Henley, S., Peltzer, G. & Simons, M., 2004. Updated Repeat Orbit Interferometry Package Released, *Eos Trans. AGU,* **85**(5), 47.

Savage, J.C. & Burford, R.O., 1973. Geodetic determination of the relative plate motion in central California, *J. Geophys. Res.,* **78,** 832–845.

Sengör, A.M.C., Görür, N. & Saroglu, F., 1985. Strike-slip faulting and related basin formation in zones of tectonic escape: Turkey as a case study, in *Strike-Slip Faulting and Basin Formation,* eds Biddle, K.T. & Christie-Blick, N., *Spec. Publ. Soc. Econ. Paleontol. Mineral.,* **37,** 227–267.

Sengör, A.M.C., Tüysür, O., Imren, C., Sakinc, M., Eyidogan, H., Görür, N., Le Pichon, X. & Rangin, C., 2004. The North Anatolian fault: a new look, *Annu. Rev. Earth Planet. Sci.,* **33,** 1–75.

Stein, R.S., Barka, A. & Dietrich, J.J., 1997. Progressive failure on the North Anatolian fault since 1939 by earthquake stress triggering, *Geophys. J. Int.,* **128,** 594–604.

Straub, C., Kahle, H.G. & Schindler, C., 1997. GPS and geologic estimates of the tectonic activity in the Marmara Sea region, NW Anatolia, *J. Geophys. Res.,* **102**(B12), 27 587–27 601.

Tatar, O. *et al.*, 2012. Crustal deformation and kinematics of the eastern part of the North Anatolian fault zone (Turkey) from GPS measurements, *Tectonophysics,* **518–521,** 55–62.

Taymaz, T., Tan, O. & Yolsal, S., 2004. Active tectonics of Turkey and surroundings and seismic risk in the Marmara Sea Region, in *The Proceedings of IWAM04,* Mizunami, Japan.

Van der Kooij, M., Hughes, W., Sato, S. & Poncos, V., 2005. Coherent target monitoring at high spatial density, examples of validation results, in *Fifth International Workshop on SAR Interferometry, 'FRINGE05',* Frascati, Italy, 28 Nov-2 Dec 2005.

Walters, R.J., Holley, R.J., Parsons, B.E. & Wright, T.J., 2011. Interseismic strain accumulation across the North Anatolian Fault from Envisat InSAR measurements, *Geophys. Res. Lett.,* **38,** L05303.

Werner, C., Wegmüller, U., Strozzi, T. & Wiesmann, A., 2003. Interferometric point target analysis for deformation mapping, *Geoscience and Remote Sensing Symposium, IGARSS 2003*.

Wessel, P. & Smith, W.H.F., 1998. New, improved version of the Generic Mapping Toolsreleased, *Eos Trans. AGU,* **79,** 579.

Wortel, M.J.R. & Spakman, W., 2000. Subduction and slab detachment in the Mediterranean-Carpathian Region, *Science,* **290,** 1910–1917.

Wright, T.J., Parsons, B.E. & Fielding, E.J., 2001. Measurement of interseismic strain accumulation across the North Anatolian Fault by satellite radar interferometry, *Geophys. Res. Lett.,* **28,** 2117–2120.

Yavasoglu, H. *et al.*, 2006. GPS measurements along the North Anatolian fault zone on the Mid-Anatolia segment, *From Geophysical to Engineering Roles,* **131,** 166–171.

Yavasoglu, H., Tari, E., Tüysüz, O., Cakir, Z. & Ergintav, S., 2011. Determining and modelling tectonic movements along the central part of the North Anatolian Fault (Turkey) using geodetic measurements, *J. Geodyn.,* **51,** 339–343.

Yolsal-Cevikbilen, S., Biryol, C.B., Beck, S., Zandt, G., Taymaz, T., Adiyaman, H.E. & Ozacar, A., 2012. 3-D crustal structure along the North

Anatolian Fault Zone in north-central Anatolia revealed by local earthquake tomography, *Geophys. J. Int.,* online version, doi:10.1111/j.1365-246X.2011.05313.x.

Yoshioka, T., Okumura, K., Kuscu, L. & Emre, O., 2000. Recent surface faulting of the North Anatolian Fault along the 1943 Ladik earthquake ruptures, *Bull. Geol. Surv. Japan,* **51**(1), 29–35.

Zebker, H.A. & Villasenor, J., 1992. Decorrelation in interferometric radar surface echoes, *IEEE Trans. Geosci. Remote Sens.,* **30**(5), 950–959.

Zebker, H.A., Rosen, P. & Hensley, S., 1997. Atmospheric effects in interferometric synthetic aperture radar surface deformation and topographic maps, *J. Geophys. Res.,* **102,** 7547–7563.

SUPPORTING INFORMATION

Additional Supporting Information may be found in the online version of this article.

Appendix (http://gji.oxfordjournals.org/lookup/supp1/doi:10.1093/gji/ggs085/-/DC1)

Please note: Oxford University Press is not responsible for the content or functionality of any supporting materials supplied by the authors. Any queries (other than missing material) should be directed to the corresponding author for the article.